Master's thesis

Measurement of ω and ϕ meson production via dimuons at forward rapidity in pp collisions at $\sqrt{s} = 13.6$ TeV with ALICE

Author : Masahiro Oida

Supervisor : Prof. Kenta Shigaki

Co-Examiner : Prof. Chiho Nonaka

Co-Examiner : Prof. Masao Kuriki

Hiroshima University
Graduate School of Advanced Science and Engineering
Physics program

Affiliation : Quark Physics Laboratory and $SKCM^2$

Contents

Abstract

As theoretically explained, hadrons that constitute matter acquire mass dynamically through spontaneous chiral symmetry breaking. The degree of chiral symmetry breaking is expressed by the vacuum expectation value of quark condensate ($< q\bar{q} >$). Since $< q\bar{q} >$ approaches zero in ultra-high temperature and high-density quark-gluon medium, chiral symmetry restoration is expected. Consequently, hadron mass changes are also considered to occur. When quarks and gluons reach an ultra-high temperature and high-density state, a phase transition from the hadron phase to the quark-gluon plasma (QGP) phase occurs. QGP can be created through high-energy heavy-ion collision experiments.In other words, chiral symmetry restoration is expected within QGP, which is generated by high-energy heavy-ion collisions. Light vector mesons are theoretically predicted to exhibit significant mass distribution changes. So far, searches for mass modifications of light vector mesons (ρ, ω, ϕ) inside QGP have been conducted using lepton pairs. Light vector mesons serve as probes for hadron mass within QGP. They decay into only lepton pairs, which do not strongly interact with QGP. Additionally, due to their relatively short lifetimes, they tend to decay inside QGP at low transverse momentum, providing information on hadron mass within QGP. However, the observed changes in the mass distribution of lepton pairs can be explained by mechanisms other than chiral symmetry restoration, and a definitive conclusion has not yet been reached.

Therefore, I aim to investigate chiral symmetry restoration by measuring muon pairs using the forward detector system of the ALICE experiment during LHC Run 3 and clarifying the transverse momentum dependence of light vector meson mass distribution changes in lead nucleus collision events. The forward region of the ALICE experiment is equipped with detectors for muon identification. Unlike electron pairs, muon pairs are not produced from π^0 Dalitz decay, and their contribution from photon (γ) conversion into electron pairs in materials is minimal. Thus, muon pair measurements offer a better signal-to-background ratio than electron pair measurements. In Run 3, a new silicon detector (MFT) was installed into the ALICE forward detectors. This enables precise measurement of the muon production point and improves the accuracy of pseudo-rapidity and azimuthal angle measurement. The MFT is expected to enhance the removal of heavy-flavour muons based on their different lifetimes, improve low transverse momentum measurement accuracy, and increase the mass resolution of muon pairs.

This master's thesis presents the transverse momentum dependence of ω, ϕ mesons yield using forward muon pairs in proton collision events from ALICE Run 3. The proton collision analysis serves as a reference for the lead nucleus collision analysis. Additionally, it plays a crucial role in evaluating and improving the new muon track reconstruction with the MFT. Track reconstruction was performed using the forward muon tracking detectors (MFT-MCH-MID), and the invariant mass distribution of muon pairs was reconstructed. A fit was applied to the extracted ω, ϕ meson peaks and their yields were calculated. The transverse momentum dependence of these yields was then determined. Along with this analysis, optimization of the matching χ^2 cut between the MFT and MCH track was conducted to minimize the statistical uncertainty of ω, ϕ yields under the current track reconstruction quality. Furthermore, an analysis was performed to remove falsely matched tracks in MFT-MCH matching. By optimizing the pseudo-rapidity difference ($\Delta\eta$) cut between the MFT and MCH track constituting a reconstructed track in the MFT-MCH-MID, the $\Delta\eta$ value that effectively removes fake match tracks was determined.

1 Introduction

1.1 QCD

The fundamental components of the matter around us are elementary particles. The behaviour of elementary particles, such as quarks and gluons, is described by quantum field theory. In particular, quarks and gluons possess degrees of freedom called color, the physics governing this degree of freedom is known as Quantum Chromodynamics (QCD). QCD is based on an SU(3) gauge theory and describes the strong interaction. QCD Lagrangian is expressed as follows:

$$\mathcal{L}_{QCD} = \sum_q \bar{\psi}_{q,a}(i\gamma^\mu \partial_\mu - m_q)\psi_{q,a} + g_s \sum_q \bar{\psi}_{q,a}\gamma^\mu T^A_{ab}\psi_{q,b}G^A_\mu - \frac{1}{4}G^A_{\mu\nu}G^{A\mu\nu} \tag{1}$$

$\psi_{q,a}$ and $\bar{\psi}q, a$ represent the quark and antiquark fields, where q denotes the flavor degree of freedom and a denotes the color degree of freedom. The γ^μ are the gamma matrices, m_q is the quark mass corresponding to each flavor, g_s is the QCD coupling constant, $T^A ab$ are the generator matrices, G^A_μ is the gluon field, and $G^A_{\mu\nu}$ is the gluon field tensor.

The first term in (1) represents the term for a free particle of mass m, the second term represents the interaction between quarks and gluons, and the third term represents the interaction between gluons themselves. A significant difference from Quantum Electrodynamics (QED), which describes electromagnetic interactions, is the presence of the coupling constant $\alpha_s(Q^2)$ and the self-interaction of the gluon field. In QED, the coupling constant does not depend on the energy scale. However, the coupling constant $\alpha_s(Q^2)$ that appears in QCD depends on the energy scale. Figure 1 shows how

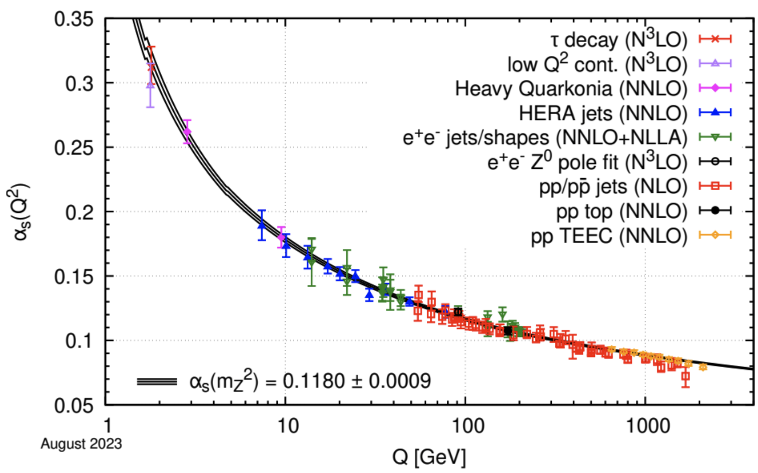

Figure 1: Q^2 dependence of QCD coupling constants

the coupling constant $\alpha_s(Q^2)$ changes with the energy scale[1]. The coupling constant becomes small at high energy scales, corresponding to short distances. This reflects the phenomenon of asymptotic freedom, where quarks behave as free particles when they are sufficiently close to each other. On the other hand, at low energy scales corresponding to long distances, the coupling constant grows infinitely large. This represents the phenomenon of quark confinement, where quarks cannot be isolated as individual particles.

Next, we focus on the gluon selfinteraction. The gluon field tensor is expressed as:

$$G^A_{\mu\nu} = \partial_\mu G^A_\nu - \partial_\nu G^A_\mu + g_s f^{ABC} G^B_\mu G^C_\nu \tag{2}$$

where f^{ABC} are the structure constants of the SU(3) group. Substituting this into the third term of (1), we obtain:

$$\begin{aligned} -\frac{1}{4}G^A_{\mu\nu}G^{A\mu\nu} &= -\frac{1}{4}(\partial_\mu G^A_\nu - \partial_\nu G^A_\mu + g_s f^{ABC}G^B_\mu G^C_\nu)(\partial^\mu G^{A\nu} - \partial^\nu G^{A\mu} + g_s f^{ABC}G^{B\mu}G^{C\nu}) \\ &= -\frac{1}{4}(\partial_\mu G^A_\nu - \partial_\nu G^A_\mu)(\partial^\mu G^{A\nu} - \partial^\nu G^{A\mu}) \\ &\qquad -g_s f^{ABC}G^B_\mu G^C_\nu \partial^\mu G^{A\nu} - g_s^2 f^{ABE}f^{CDE}G^A_\mu G^B_\nu G^{C\mu}G^{D\nu} \end{aligned} \tag{3}$$

In (3), the first term represents the free gluon field without interactions. The second term represents interactions involving three gluon fields, representing reactions such as $g + g \to g$. The third term corresponds to interactions involving four gluon fields, representing reactions such as $g + g \to g + g$. For photons, the third term in (2) does not exist, so the second and third terms in (3) do not appear. This is because gluons interact with each other due to their color degrees of freedom, which gives rise to gluon selfinteraction.

These characteristics—namely, the coupling constant's energy dependence and the gluons' selfinteraction—contribute to the complex structure of the quark-gluon interactions.

1.2 Chiral symmetry

The quark field can be separated into its right-handed and left-handed components. The projection operators for the right-handed and left-handed components are defined as P_R and P_L, respectively. Using the $\gamma_5 = i\gamma_0\gamma_1\gamma_2\gamma_3$ matrices, they are expressed as follows:

$$P_R = \frac{1+\gamma_5}{2}, \quad P_L = \frac{1-\gamma_5}{2} \tag{4}$$

(4) hold for these projection operators.

$$P_R + P_L = 1, \quad P_R P_L = 0, \quad P_R^2 = P_R, \quad P_L^2 = P_L \tag{5}$$

The right-handed quark field q_R and the left-handed quark field q_L are expressed using the projection operators as follows:

$$q_R = P_R q, \quad q_L = P_L q \tag{6}$$

These components are applied to the QCD Lagrangian:

$$\mathcal{L}_{QCD} = \sum_q \bar{q}(i\gamma^\mu D_\mu - m)q \tag{7}$$

- Kinetic Term (the first term of the QCD Lagrangian)

$$\bar{q}(i\gamma^\mu D_\mu)q = \bar{q}(i\gamma^\mu D_\mu)\big(P_R^2 + P_L^2\big)q \tag{8}$$
$$= \bar{q}P_L(i\gamma^\mu D_\mu)P_R q + \bar{q}P_R(i\gamma^\mu D_\mu)P_L q \tag{9}$$
$$= \bar{q}_R(i\gamma^\mu D_\mu)q_R + \bar{q}_L(i\gamma^\mu D_\mu)q_L \tag{10}$$

- Mass Term (the second term of the QCD Lagrangian)

$$\bar{q}mq = \bar{q}m\big(P_R^2 + P_L^2\big)q \tag{11}$$
$$= \bar{q}P_R m P_R q + \bar{q}P_L m P_L q \tag{12}$$
$$= \bar{q}_L m q_R + \bar{q}_R m q_L \tag{13}$$

From the above, the kinetic term of the quark field can be separated into the right-handed and left-handed quark fields, thereby preserving chiral symmetry. However, the mass term mixes the right-handed and left-handed quark fields, breaking chiral symmetry. Considering the chiral limit ($m_q = 0$), the QCD Lagrangian preserves chiral symmetry.

The degree of chiral symmetry breaking is expressed as the vacuum expectation of quark condensation $< \bar{q}q >$. As shown in Figure 2[2], this quantity takes a finite value in the ground state of hadrons at standard temperature and density. But, it is expected to approach $< \bar{q}q > \sim 0$ at extremely high temperatures and densities. Since the vacuum expectation value of the quark condensate cannot be directly measured, as described later, various other probes are used to investigate the restoration of chiral symmetry.

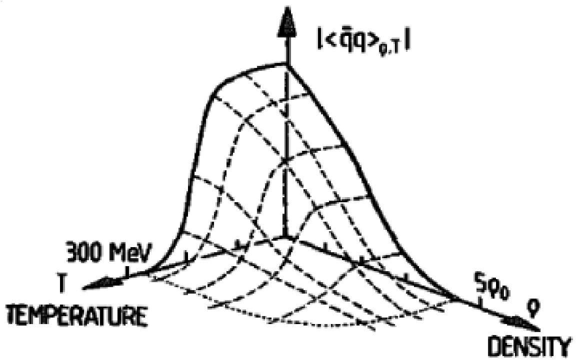

Figure 2: Temperature and density dependence of the expected value of quark condensation

1.3 NJL model

The interaction between quarks and gluons, as described in 1.1, exhibits a complex structure, making it difficult to understand various phenomena from first-principle calculations. Therefore, models are employed to describe various phenomena. One such model is the Nambu-Jona-Lasinio (NJL), a chiral effective model. Its Lagrangian is expressed as follows.

$$\mathcal{L} = \bar{q}i\gamma \cdot \partial q - (-g)\left[(\bar{q}q)^2 + (\bar{q}i\gamma_5 q)^2\right] \tag{14}$$

where, q and $\bar{q}$ represent quark and antiquark fields, respectively; γ and γ_5 are gamma matrices, with $\gamma_5 = i\gamma_0\gamma_1\gamma_2\gamma_3$. Since there is an attractive force between quarks and antiquarks, the coupling constant g is positive and has a dimension of $[\text{mass}]^{-2}$. This model is an effective chiral theory for QCD at the energy scale of 1 GeV. To determine the ground state of this Lagrangian, the self-consistent mean field approximation (MFA) is employed:

$$\langle \bar{q}q \rangle \equiv \frac{-m_0^2 \sigma}{G} \tag{15}$$

$$\langle \bar{q}i\gamma_5 q \rangle \equiv \frac{-m_0^2 \pi}{G} \tag{16}$$

By substituting (15) and (16) into (14), the expression is reformulated. Defining $\sigma = \bar{q}q$, $\pi = \bar{q}i\gamma_5 q$, and $2g = (G/m_0)^2$, we get:

$$\mathcal{L}_{MFA} = \bar{q}[i\gamma \cdot \partial - G(\sigma + i\pi\gamma_5)]q - \frac{m_0^2}{2}\left(\sigma^2 + \pi^2\right) \tag{17}$$

where, defining $q_\theta = e^{i\gamma_5 \frac{\theta}{2}} q$, $G\sqrt{\sigma^2+\pi^2} = M$, and $\pi/\sigma = \tan\theta$, the Hamiltonian can be expressed as follows. θ is the parameter of the chiral transformation.

$$H_{MFA} = \int \mathrm{d}^3\boldsymbol{x} \left\{ \bar{q}_\theta(x)(-i\gamma\cdot\nabla + M)q_\theta(x) + \frac{m_0^2}{2}\sigma_0^2 \right\} \tag{18}$$

where $\sigma_0^2 = \sigma^2 + \pi^2$. Since π is considered sufficiently small, we write σ to σ_0. From this Hamiltonian, the Dirac equation for mass M can be derived. Its solution is given as (19).

$$q_\theta(x) = \frac{1}{\sqrt{V}} \sum_{\boldsymbol{p},r=\pm} \sqrt{\frac{M}{E_p}} \left\{ a_M(\boldsymbol{p},r)u_M(\boldsymbol{p},r)e^{-ip\cdot x} + b_M^\dagger(\boldsymbol{p},r)v_M(\boldsymbol{p},r)e^{ip\cdot x} \right\} \tag{19}$$

where, r represents helicity, $E_p = \sqrt{\boldsymbol{p}^2 + M^2}$, and $M = -g\langle \bar{q}_\theta q_\theta \rangle$. Next, when $q_\theta(x)$ is expanded using spinors with zero mass, the solution is:

$$q_\theta(x) = \frac{1}{\sqrt{V}} \sum_{\boldsymbol{p},s=R,L} \left\{ a_{\boldsymbol{p}}^{(s)}(t)u_0(\boldsymbol{p},s)e^{-i\boldsymbol{p}\cdot\boldsymbol{x}} + b_{\boldsymbol{p}}^{(s)\dagger}(t)v_0(\boldsymbol{p},s)e^{i\boldsymbol{p}\cdot\boldsymbol{x}} \right\} \tag{20}$$

where s represents helicity. Using the solutions (19) and (20), the Hamiltonian (18) can be expressed in terms of operators for massive and massless states. Here, $a_{\boldsymbol{p}}$ and $b_{\boldsymbol{p}}$ are expansion coefficients:

$$\begin{aligned} H_{MFA} = \sum_{\boldsymbol{p},s} &\left\{ |\boldsymbol{p}| \left(a_{\boldsymbol{p}}^{(s)\dagger}(t)a_{\boldsymbol{p}}^{(s)}(t) - b_{-\boldsymbol{p}}^{(s)}(t)b_{-\boldsymbol{p}}^{(s)\dagger}(t) \right) \right\} \\ &+ M\left(b_{-\boldsymbol{p}}^{(s)}(t)a_{\boldsymbol{p}}^{(s)}(t) + a_{\boldsymbol{p}}^{(s)\dagger}(t)b_{-\boldsymbol{p}}^{(s)\dagger}(t) \right) + V\frac{m_0^2}{2}\sigma_0^2 \qquad (21) \\ = &\sum_{\boldsymbol{p},r} E_p \left(a_M^\dagger(\boldsymbol{p},r)a_M(\boldsymbol{p},r) - b_M(\boldsymbol{p},r)b_M^\dagger(\boldsymbol{p},r) \right) + V\frac{m_o^2}{2}\sigma_0^2 \qquad (22) \end{aligned}$$

From this Hamiltonian, the following Heisenberg equation can be derived:

$$i\begin{pmatrix} \dot{a}_{\boldsymbol{p}}^{(s)}(t) \\ \dot{b}_{-\boldsymbol{p}}^{(s)}(t) \end{pmatrix} = \begin{pmatrix} |\boldsymbol{p}| & M \\ M & -|\boldsymbol{p}| \end{pmatrix} \begin{pmatrix} a_{\boldsymbol{p}}^{(s)}(t) \\ b_{-\boldsymbol{p}}^{(s)}(t) \end{pmatrix} \tag{23}$$

Setting the initial state $a_{\boldsymbol{p}}^{(s)}(t=0) = a_{M=0}(\boldsymbol{p},s)$, the solution reveals that the massive and massless operators are connected via the Bogoliubov transformation:

$$\begin{pmatrix} a_M(\boldsymbol{p},r) \\ b_M(\boldsymbol{p},r)^\dagger \end{pmatrix} = U(\boldsymbol{p},r)\begin{pmatrix} a_0(\boldsymbol{p},r) \\ b_0(\boldsymbol{p},r)^\dagger \end{pmatrix} U^\dagger(\boldsymbol{p},r) \tag{24}$$

where $U(\boldsymbol{p},r) = \exp\left\{ -\frac{\theta_p}{2}(a_0^\dagger(\boldsymbol{p},r)b_0^\dagger(-\boldsymbol{p},r) - b_0(-\boldsymbol{p},r)a_0(\boldsymbol{p},r)) \right\}$. The vacuum states for each operator are defined as follows:

$$|\sigma_0\rangle \quad \to \quad a_M(\boldsymbol{p},r)|\sigma_0\rangle = b_M(\boldsymbol{p},r)|\sigma_0\rangle = 0 \tag{25}$$

$$|0\rangle \quad \to \quad a_0(\boldsymbol{p},r)|0\rangle = b_0(\boldsymbol{p},r)|0\rangle = 0 \tag{26}$$

$a_0(\boldsymbol{p},r)^\dagger$ creates an eigenstate of chirality, while $a_M(\boldsymbol{p},r)^\dagger$ creates an eigenstate of helicity. Based on the vacuum definition and (24), acting on $|0\rangle$ produces an eigenstate of helicity but not a definite chirality eigenstate. This implies that "chiral symmetry is spontaneously broken".

Thus, the NJL model theoretically predicts vacuum phase transitions. In our universe, it is believed that quark condensation spontaneously breaks chiral symmetry, leading to hadrons acquiring significant masses.

1.4 Quark-Gluon Plasma

When hadrons are exposed to extremely high temperatures and densities, they transition into a plasma state known as the Quark-Gluon Plasma (QGP). In the QGP, quarks are resolved from confinement, and chiral symmetry restoration is also expected. Furthermore, it is believed that the universe was in a QGP state immediately following the Big Bang. On the QCD phase diagram, which represents the phase structure of quarks and gluons, the QGP phase appears as shown in Figure 3. The QGP phase can be observed in high-temperature regions in both high net baryon density and

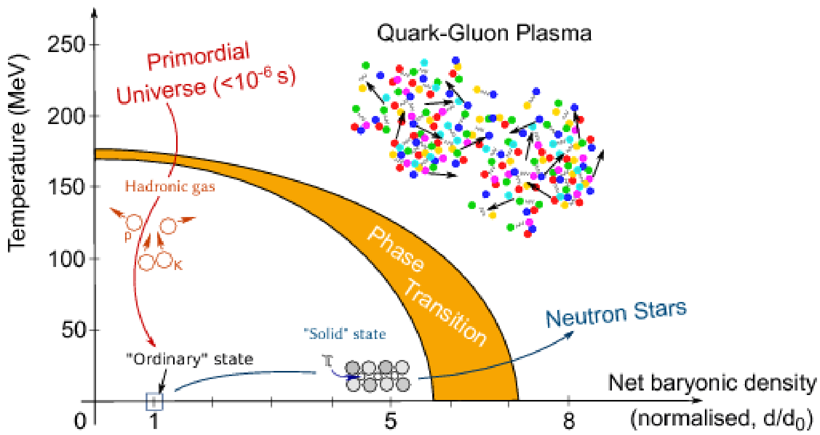

Figure 3: QCD Phase Diagram[3]

low net baryon density areas. Two types of phase transitions are involved in the transition to the QGP phase. The first is the chiral phase transition. The second is the deconfinement-confinement phase transition.

The chiral phase transition is the spontaneous breaking of chiral symmetry as the vacuum undergoes a phase transition, allowing quarks to acquire a substantial effective mass. In other words, the chiral phase transition is deeply related to the mass acquisition of hadrons. The deconfinement–confinement phase transition pertains to the confinement of quarks. In the hadronic ground state, quarks are confined by color interaction. However, in the QGP state, quarks are resolved from confinement and transition into a plasma state. This is the deconfinement-confinement phase transition. While these transitions are believed to occur at approximately a similar critical temperature, this relationship is not fully understood, and research is ongoing.

1.5 Heaby Ion collision

The existence of the QGP, which is ultrahigh-temperature or dense matter, has been confirmed by heavy-ion collision experiments. Figure 4 shows the time evolution proceeds in the following.

1. Pre-equilibrium state
2. QGP
3. Hadronization
4. Kinetic Freeze-out

In the initial stage of the collision, partons from the nucleons undergo elastic and deep inelastic scatterings to reach thermalisation. During this initial collision, phenomena such as jet production

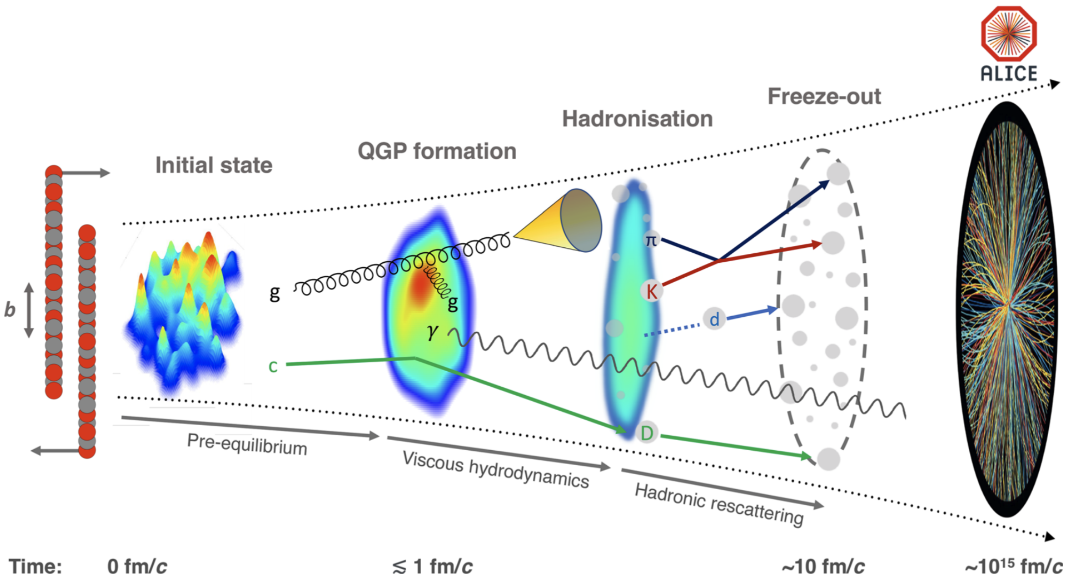

Figure 4: The evolution of a heavy-ion collision at LHC energies[4]

and the pair production of heavy quarks occur. Once the matter generated in the collision region reaches thermal equilibrium, the system transitions into the QGP state.

In the QGP state, photons and lepton pairs originating from the thermal radiation of high-temperature matter are generated. Jets interact with the QGP and lose energy, resulting in jet quenching, while heavy quarks undergo deconfinement due to the color Debye screening. Subsequently, as the QGP cools, hadronisation occurs, leading to chemical freeze-out.

Chemical freeze-out refers to the cessation of changes in particle species due to deep inelastic scatterings among particles. However, elastic scatterings between hadrons continue, allowing momentum exchange among particles. Later, kinetic freeze-out occurs, fixing the momenta and other properties of the particles. The particles finally detected are those that remain after the kinetic freeze-out. Thus, the QGP is formed during the temporal evolution of heavy-ion collisions, and its lifetime is extremely short.

The QGP generated in heavy-ion collisions has its density and temperature determined by the collision energy. High-density QGP regions are realised at collision energies of $\sqrt{s_{NN}} \lesssim 10$ GeV. At these energies, the colliding particles stop at the collision point. Creating a high-density state where kinetic energy is converted directly into heat, increasing the temperature.

On the other hand, high temperature and low net baryon density regions are achieved at collision energies of $\sqrt{s_{NN}} \gtrsim 100$ GeV. In this energy regime, the colliding particles do not stop but pass through each other, producing numerous particle-antiparticle pairs. As a result, the baryon number density does not become large relative to the temperature. However, the high energy density in this region leads to the creation of high-temperature matter near the collision point.

In the ALICE experiment, LHC Run 3 operations began in 2022, initiating Pb-Pb collision measurements at $\sqrt{s_{NN}} = 5.36$ TeV. This collision energy produces QGP in the ultrahigh-temperature, low net baryon density region. Moreover, compared to the QGP generated at $\sqrt{s_{NN}} = 200$ GeV at RHIC, the higher collision energy at the LHC enables the measurement of a larger QGP than ever before.

1.6 Dilepton Measurement

Dilepton measurement is a sensitive probe for investigating the time evolution of heavy-ion collisions. Since leptons do not participate in strong interactions, they are minimally affected by the QGP. This property allows for the measurement of a dilepton distribution that integrates contributions from all stages of heavy-ion collisions. The sources of dilepton production are illustrated in Figure 5.

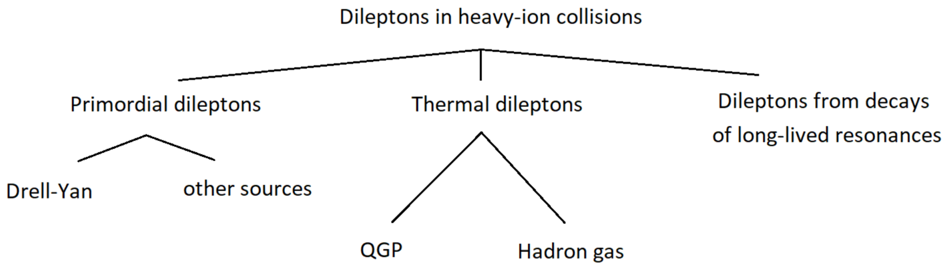

Figure 5: Dilepton source[5]

- Primordial dileptons (from $q\bar{q}$ annihilation)
- Thermal dileptons
- Dileptons from hadron decays

The dilepton mass regions correspond to different stages in the time evolution of heavy-ion collisions. In the High-Mass Region, primordial dileptons from the Drell-Yan process constitute the continuum

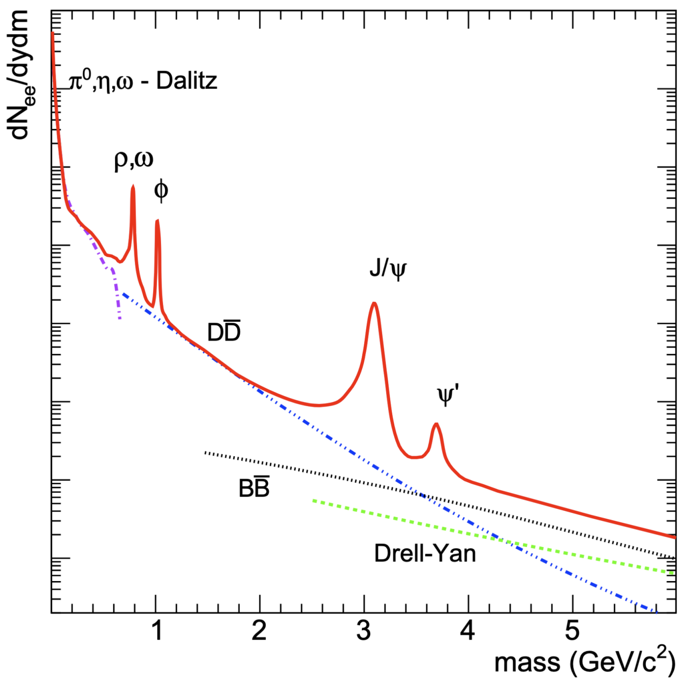

Figure 6: Expected mass spectrum from dileptons[7]

component of the mass distribution, reflecting the initial state of the collision. In the Intermediate-Mass Region, thermal dileptons originating from the QGP, as well as continuum components such as open-charm and open-beauty decays, are observed.

Finally, in the Low-Mass Region, the dilepton distribution is predominantly derived from light meson decays in the hadronic gas. Most dileptons from hadron decays originate from mesons with relatively long lifetimes, meaning they primarily reflect the hadronic gas phase. However, light vector mesons (ρ, ω, ϕ) have extremely short lifetimes, making them sensitive to the QGP effects.

1.7 Search for chiral symmetry restoration in QGP

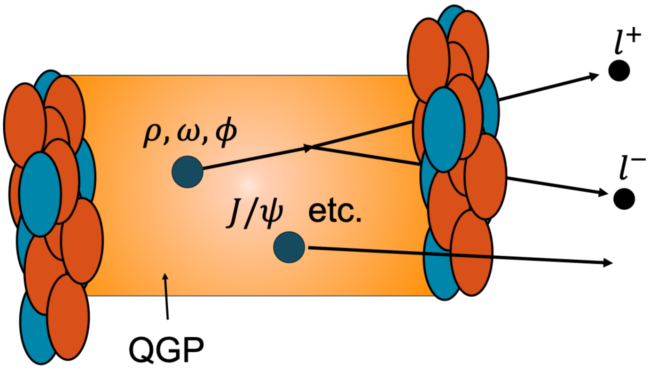

Figure 7: Low mass vector meson decay in QGP

In the QGP, an ultra-high temperature and high-density state is expected to be realised, leading to $< \bar{q}q >\sim 0$ and restoring chiral symmetry. Light vector mesons (ρ, ω, ϕ) serve as probes for the masses of hadrons in the QGP. These particles have short lifetimes and decay channels into dileptons. As shown in Figure 7, their short lifetimes make it possible for them to decay within the QGP, before hadronization occurs. Additionally, since they decay into only dileptons, which do not interact via the strong force with the QGP, the masses of hadrons within the QGP can be measured.

In past experiments, dilepton measurements have been used to investigate chiral symmetry restoration. In the SPS-NA60 experiment, the excess of muon pairs in the low-mass region was reported. However, the excess could also be explained by the process $\pi\pi \to \rho \to \pi\pi$; thus, it did not serve as definitive evidence of chiral symmetry restoration[8].

Additionally, in the electron pair measurements during ALICE Run 2 $\sqrt{s_{NN}} = 5.02$ TeV lead-lead collisions, contributions from open-charm and open-beauty were estimated along with the vacuum dilepton distribution excluding ρ, and an excess of electron pairs was reported. The excess was explained as thermal dileptons from the QGP, consistent with the error range[6].

1.8 Analysis of pp collision data as a baseline

This paper presents the analysis results of proton-proton collision events. The particles generated in proton-proton collisions are produced from the vacuum. Measurements of such events, where no QGP is formed, serve as a baseline for comparison with events where QGP is generated. Currently, the quality of track reconstruction remains insufficient, and the muon pair analysis is incomplete. Moreover, muon track reconstruction in heavy-ion collisions is even more challenging than in proton-proton collisions due to the significantly larger number of particles produced per event.

The purpose of this study is to provide an analysis as a baseline for future studies of $\sqrt{s_{NN}} = 5.02$ TeV lead-lead collisions, where QGP is expected to be generated and to improve the quality of muon tracks in ALICE Run 3 $\sqrt{s} = 13.6$ TeV proton-proton collisions.

2 Detector setup

2.1 Large Hadron Collider

The Large Hadron Collider (LHC) is the world's largest circular accelerator. Figure 8 shows that the LHC and its major experimental collaborations are located near Geneva, Switzerland. LHC Run 1 was conducted from 2009 to 2013, and Run 2 followed from 2015 to 2018. The ongoing Run 3 is scheduled to collect physics data from 2022 to the summer of 2026. During this period, most measurements focus on proton-proton collisions, with heavy-ion collision measurements conducted for about one month each year. The LHC hosts four major experimental collaborations: ATLAS, CMS, LHCb, and ALICE.

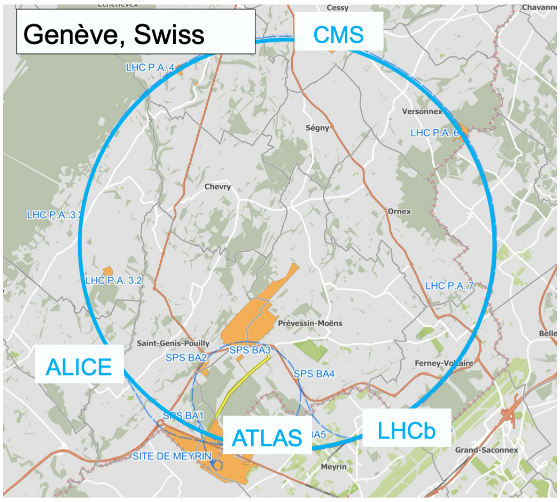

Figure 8: LHC

2.2 A Large Ion Collider Experiment

The A Large Ion Collider Experiment (ALICE) collaboration is an international effort of 168 research institutions from 40 countries and approximately 2,000 researchers. The overall view of the ALICE detector is shown in Figure 9. The ALICE detector system is dedicated to studying the Quark-Gluon Plasma (QGP) produced in heavy-ion collisions. The detectors can be broadly divided into

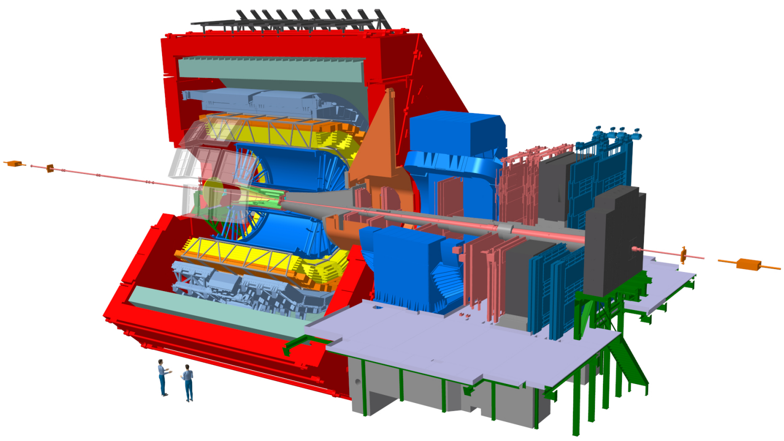

Figure 9: ALICE detectors

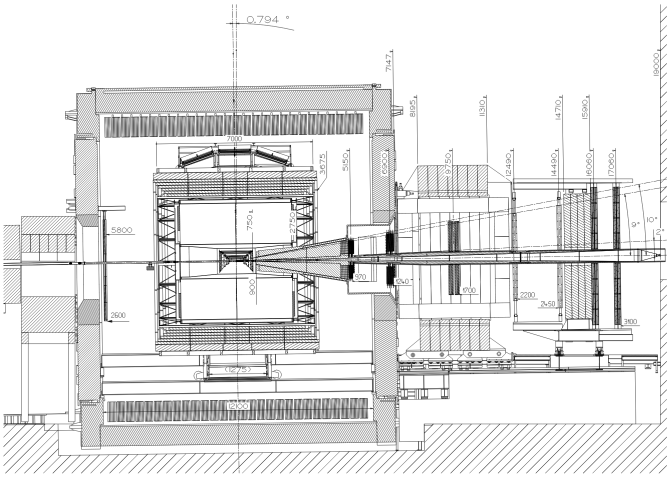

Figure 10: MUON spectrometer

two main groups: the barrel detectors and the forward detectors. The barrel detectors include ITS, TPC, TOF, EMCal, TRD, PHOS/CPV, and HMPID detectors. A magnetic field is applied along the beam axis, bending the motion of charged particles and enabling particle identification, momentum, and energy measurements. The forward detectors are specifically designed for muon measurements and consist of three trackers—MFT, MCH, and MID—and two hadron absorbers. A dipole magnet is placed between MCH, allowing the measurement of muon momentum and sign. Other detectors include the ZDC and FIT. The ZDC is located far from the collision point and measures the number of neutrons and protons, determining the centrality of heavy-ion collision events. The FIT detectors are located forward and backward near the collision point to measure the event luminosity and particle multiplicity.

2.2.1 MUON Spectrometer

The MUON spectrometer is shown in Figure 10[10]. The MUON spectrometer consists of the Front Absorber, MCH, Iron Wall, and MID with an acceptance range of $-4.0 < \eta < -2.5$. It utilizes the high penetration power of muons for their identification. Various particles generated at the collision point (IP) pass through the Front Absorber. Hadrons and light electrons, which interact strongly, are absorbed by the Front Absorber, while the muons, due to their high penetration power, pass through it. The muons that pass through the Front Absorber are detected, and any particles such as π mesons produced from interactions within the Front Absorber are measured by the MCH. These particles are absorbed in the Iron Wall, preventing the MID from detecting them. Therefore, muon identification is performed by combining tracks measured in the MCH and MID. The momentum of the muons is measured using a dipole magnet in the MCH, which is set to a magnetic flux density of 3.0 $\mathrm{T/m^2}$.

2.2.2 MFT

The MUON spectrometer is shown in Figure 11[9]. The MFT is a newly installed silicon pixel detector positioned between $z = -46.0$ and $z = -76.8$ cm, with an acceptance range of $-3.6 < \eta < -2.5$ in Run 3. It consists of five layers of disks that detect tracks and reconstructs standalone MFT tracks, taking into account the influence of the L3 magnet, which generates the ALICE central magnetic field. Since the detector is placed in front of the Front Absorber, the measured tracks include muons

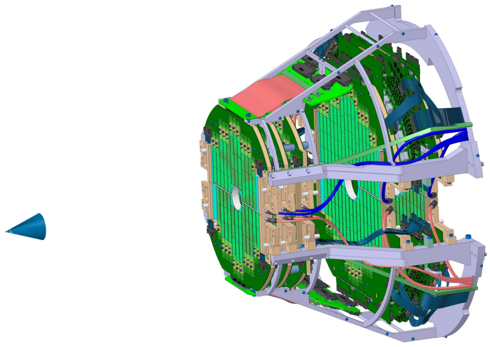

Figure 11: MFT

as well as various other particles, such as π mesons and K mesons. By combining these tracks with those measured by the backward MUON spectrometer, the DCA of the muons can be determined. This capability allows for the separation of muons originating from c and b quarks, based on lifetime differences. Additionally, the precision of the opening angle between the muon pair is improved, enhancing mass resolution. Furthermore, since the MFT is positioned in front of the Front Absorber, it allows for the measurement of muons with lower transverse momentum compared to those measured by the MUON spectrometer alone.

2.2.3 MFT-MUON Track Matching

The Global Track was reconstructed using the MCH track measured by the MUON spectrometer and the MFT track measured by the MFT detector. First, the MCH tracks measured by the MUON spectrometer are extrapolated toward the collision point, extending up to the last disk of the MFT, located at $z = 76.8$ cm. This extrapolation accounts for multiple scattering and energy loss corrections in the Front Absorber, which is located between the MUON spectrometer and the MFT. Next, suitable MFT tracks are selected based on both their position and direction, and the matching quality is evaluated by comparing the position and slope of the tracks. The MFT track with the best matching quality is selected and used to construct the Global Track.

3 Analysis

3.1 DataSet

The data used is a subset of pp collisions at $\sqrt{s} = 13.6$ TeV, collected in 2022. The collision rate for pp is 500 kHz, and the dataset is labeled LHC22o_apass7. The Monte Carlo simulation data used in 3.6.2 employs Pythia8 Monash to reproduce 500 kHz pp collisions at $\sqrt{s} = 13.6$ TeV, utilizing minimum bias event simulations without extracting specific events.

3.2 Event selection

The ITS detector system measured the position of the proton-proton collision. The Z-coordinate of the collision point, denoted as VtxZ, was selected with the condition $|VtxZ| < 10$ cm, using the ITS centre at Z = 0 as the reference. This cut value is adjusted based on the ITS acceptance. The number of events obtained after applying this cut is 5.5×10^9.

3.3 Single muon track reconstruction

The Global Track, reconstructed in 2.2.3, was used to calculate the physical quantities of the muon as follows. The MFT track measures the muon's η and ϕ. The momentum p was derived by propagating the MCH standalone track to the Z-coordinate of the collision point, with corrections applied for multiple scattering and energy loss in the absorber. For the DCA, a global fit was performed for all tracks constituting the Global Track, and the resulting track was used. As shown in Figure 12, the track was linearly extrapolated to the Z-coordinate of the collision point (IP), and the distance between the extrapolated point and the collision point was calculated as the DCA. Similarly, using the same track, R_{abs} was calculated as the distance from the beam axis at the back edge of the absorber, as shown in Figure 13. Furthermore, the MFT-MCH matching χ^2 was calculated based on the parameter differences when extrapolating both the MFT track and MCH track to the matching plane.

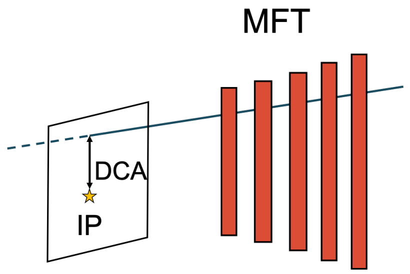

Figure 12: conceptual scheme of DCA

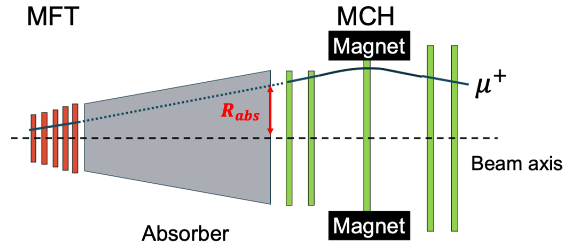

Figure 13: conceptual scheme of R_{abs}

3.4 Single muon selection

The cuts applied to the obtained Global Tracks are as follows:

- -3.6 $<\eta <$ -2.5
- 17.5 cm $< R_{abs} <$ 89.5 cm
- $pDCA < 6\sigma$
- MFT-MCH matching $\chi^2 < 30$

The η cut is adjusted to match the MFT-MCH-MID acceptance. The cut value of R_{abs} is chosen to remove tracks in regions where hadron absorbers are not present. The $pDCA$, defined as the product of momentum and DCA, is used to eliminate muons originating from beam-gas interactions. The cut was applied at 6σ based on a Gaussian fit to the $pDCA$ distribution. The MFT-MCH matching χ^2 value was optimized to minimize the statistical uncertainty in the ω and ϕ yields, as described below. The MFT-MCH matching χ^2 values were obtained from a fit to the data points detected when matching MFT and MCH tracks. The values used in this study were optimized to minimize the statistical uncertainty in the ω and ϕ yields, as discussed in 3.6.1.

3.5 Dimuon analysis

3.5.1 Dimuon reconstruction

Dimuons are reconstructed using the single muons selected in 3.4. The mass($M_{\mu\mu}$), transverse-momentum($p_{T\mu\mu}$), pseudorapidity($\eta_{\mu\mu}$), and Azimuth angle($\phi_{\mu\mu}$) of the dimuon are calculated as

(27)∼(34). First, the p_T, η, and ϕ of the single muons are converted into four-component vectors (p_x, p_y, p_z, E) using (27),(28),(29),(30).

$$\begin{aligned} p_x &= p_T\cos(\phi) \quad (27) \\ p_y &= p_T\sin(\phi) \quad (28) \\ p_z &= p_T\sinh(\eta) \quad (29) \\ E &= \sqrt{p_T^2\cosh^2(\eta) + m_\mu^2} \quad (30) \end{aligned}$$

Then, using the (p_x, p_y, p_z, E) of the single muons, the $(p_{x\mu\mu}, p_{y\mu\mu}, p_{z\mu\mu}, E_{\mu\mu})$ of the dimuon are calculated.

$$\begin{pmatrix} p_{x\mu\mu} \\ p_{y\mu\mu} \\ p_{z\mu\mu} \\ E_{\mu\mu} \end{pmatrix} = \begin{pmatrix} p_{x1} \\ p_{y1} \\ p_{z1} \\ E_1 \end{pmatrix} + \begin{pmatrix} p_{x2} \\ p_{y2} \\ p_{z2} \\ E_2 \end{pmatrix} \quad (31)$$

Using the obtained four-component vector of the dimuon $(p_{x\mu\mu}, p_{y\mu\mu}, p_{z\mu\mu}, E_{\mu\mu})$, the pair's $M_{\mu\mu}$, $p_{T\mu\mu}$, and $\eta_{\mu\mu}$ were calculated from the (32),(33),(34).

$$\begin{aligned} M_{\mu\mu} &= \sqrt{E_{\mu\mu}^2 - (p_{x\mu\mu}^2 + p_{y\mu\mu}^2 + p_{z\mu\mu}^2)} \quad (32) \\ p_{T\mu\mu} &= \sqrt{p_{x\mu\mu}^2 + p_{y\mu\mu}^2} \quad (33) \\ \eta_{\mu\mu} &= \frac{1}{2}\log\left(\frac{|\vec{p}| + p_{z\mu\mu}}{|\vec{p}| - p_{z\mu\mu}}\right) \quad (34) \\ \phi_{\mu\mu} &= \arctan\left(\frac{p_y}{p_x}\right) \quad (35) \end{aligned}$$

Using (32),(33),(34) and (35), the physical quantities of the dimuon are calculated.

3.5.2 Combinatorial background subtraction

The dimuon was reconstructed by pairing oppositely charged muons within each event. In cases with multiple possible pairings, all combinations were considered to reconstruct the physical quantities of the dimuon. Since all combinations are included, the mass distribution of uncorrelated muon pairs is also reconstructed. This component is referred to as the combinatorial background. This study employs the Like-Sign method to subtract the combinatorial background. The Like-Sign method estimates the combinatorial background using the mass distribution of same-sign muon pairs from each collision event. A key feature of this method is that it estimates the shape of the uncorrelated background using like-sign muons from the same event, enabling the subtraction of mass distributions associated with weakly correlated particles, such as those influenced by elliptic flow in heavy-ion collisions. The estimated uncorrelated background depends on the p_T of the dimuon. The calculation formula is given in (36).

$$\frac{\mathrm{d}N_{sig}}{\mathrm{d}m} = \frac{\mathrm{d}N_{same}^{+-}}{\mathrm{d}m} - 2R\sqrt{\frac{\mathrm{d}N_{same}^{++}}{\mathrm{d}m}\frac{\mathrm{d}N_{same}^{--}}{\mathrm{d}m}} \quad (36)$$

$$2R = \frac{\frac{\mathrm{d}N_{mix}^{+-}}{\mathrm{d}m}}{\sqrt{\frac{\mathrm{d}N_{mix}^{++}}{\mathrm{d}m}\frac{\mathrm{d}N_{mix}^{--}}{\mathrm{d}m}}} \quad (37)$$

Where, $\frac{\mathrm{d}N_{sig}}{\mathrm{d}m}$ represents the number of correlated muons at each mass, $\frac{\mathrm{d}N_{same}^{**}}{\mathrm{d}m}$ represents the number of same-sign muon pairs in the same event (** corresponds to the muon sign), and $\frac{\mathrm{d}N_{mix}^{**}}{\mathrm{d}m}$ represents the number of muon pairs formed from different events. R is a term to correct for the acceptance difference due to the muon sign. $R = 1$ when there is no difference in acceptances by sign. Since muon pairs from different events were not reconstructed in this analysis, $R = 1$ was used for the calculation.

The result of the combinatorial background subtraction in the dimuon transverse momentum region of $1 < p_{T\mu\mu} < 30$ GeV/c is shown in Figure 14.

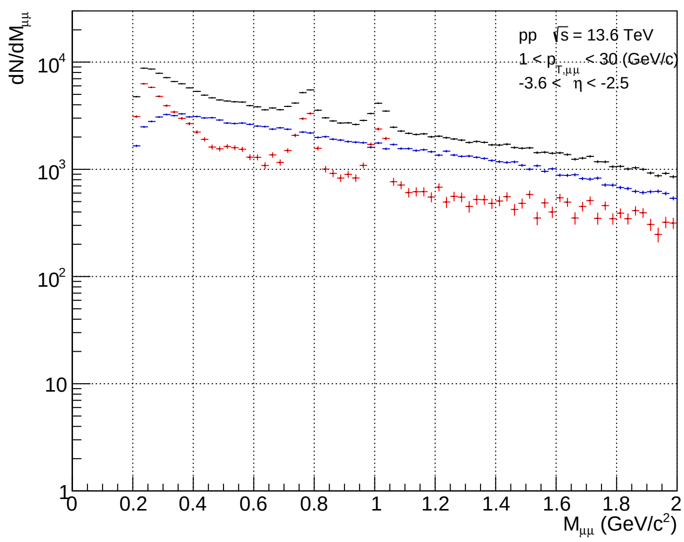

Figure 14: Dimuon invariant mass distribution with transverse momentum $1 < p_T < 30$ GeV/c minus uncorrelated background events. Black is the reconstructed invariant mass distribution for all combinations of muons of different signs in the same event. Blue is the uncorrelated background event estimated using the Like Sign method. Red is the correlated muon vs invariant mass distribution obtained by subtracting blue from black.

The horizontal axis represents the invariant mass, while the vertical axis indicates the number of dimuons per mass bin. The black distribution represents the invariant mass spectrum reconstructed by pairing oppositely charged muons from all possible combinations within the same event, while the blue distribution denotes the uncorrelated background estimated using the Like-Sign method. The red distribution, obtained by subtracting the blue from the black, represents the correlated dimuon invariant mass spectrum. The mass spectra were categorized by dimuon $p_{T\mu\mu}$, and the uncorrelated background was subtracted using the Like-Sign method in each spectrum to investigate the transverse momentum dependence of the ω and ϕ yields. Figure 15 presents the subtracted spectra.

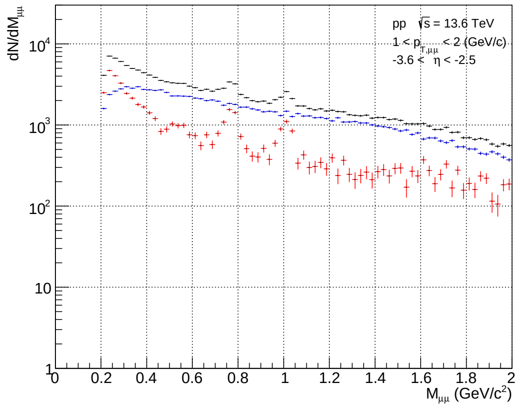

$1 < p_{T\mu\mu} < 2$ GeV/c

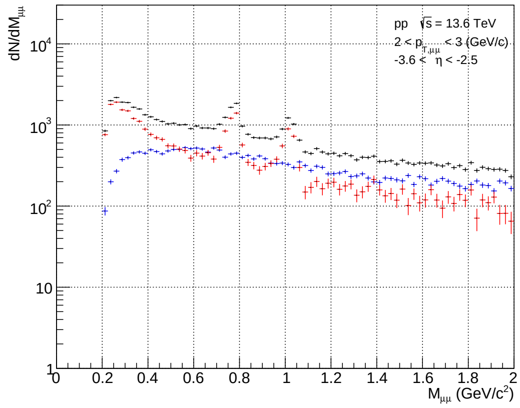

$2 < p_{T\mu\mu} < 3$ GeV/c

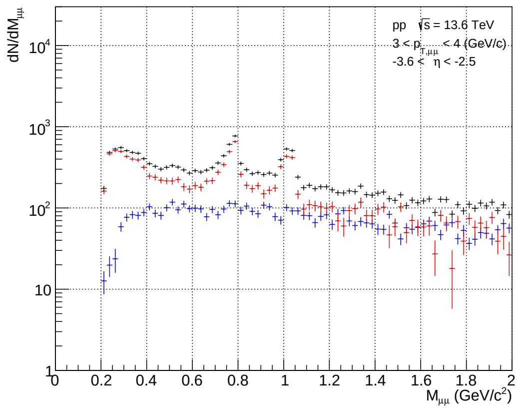

$3 < p_{T\mu\mu} < 4$ GeV/c

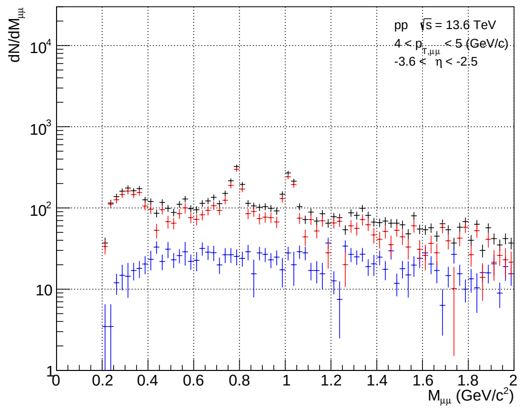

$4 < p_{T\mu\mu} < 5$ GeV/c

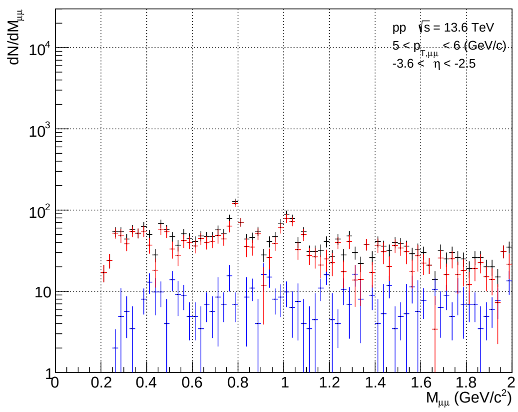

$5 < p_{T\mu\mu} < 6$ GeV/c

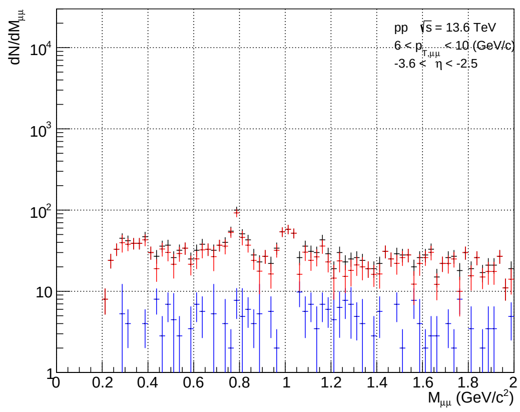

$6 < p_{T\mu\mu} < 10$ GeV/c

Figure 15: Dimuon invariant mass distribution subtracting each dimuon transverse momentum uncorrelated background event. Black is the reconstructed invariant mass distribution for all combinations of muons of different signs in the same event. Blue is the uncorrelated background event estimated using the Like Sign method. Red is the correlated muon vs invariant mass distribution obtained by subtracting blue from black.

In the region $0 < p_{T\mu\mu} < 1$ GeV/c, no peaks of ω and ϕ were observed. The reason is believed to be the insufficient resolution of the single muon p_T and the dominance of tracks with incorrect MFT-MCH matching. The region of $6 < p_{T\mu\mu} < 10$ GeV/c was chosen to be wider than other transverse momentum regions to preserve the statistical significance.

3.5.3 Peak extraction of $\omega \to \mu\mu, \phi \to \mu\mu$

The distributions of the correlated dimuon invariant mass obtained from 3.5.2 are used to extract the distributions of $\omega \to \mu\mu$ and $\phi \to \mu\mu$. The dimuon invariant mass distribution under 2(GeV/c^2) contains pairs of muons coming from light and open heavy-flavor mesons. Charm(c) and bottom(b) quarks have heavy masses produced through pair creation in the initial collision. The pair-created $c\bar{c}$ quarks separate and form $D\bar{D}$ mesons. The D and $\bar{D}$ mesons undergo semileptonic decays, such as $D \to \bar{K}^0 + \mu^+ + \nu_\mu$ or $D \to \mu^+ + \nu_\mu$, and $\bar{D} \to K^0 + \mu^- + \nu_\mu$ or $\bar{D} \to \mu^- + \nu_\mu$. Since the parent D and $\bar{D}$ mesons are produced through pair creation, they are strongly correlated, and their decay products, the muons, also exhibit correlation. As a result, the dimuon mass distribution with correlations is included. The same correlation applies in the case of B mesons.

- $\eta \to \mu^+\mu^-$
- $\eta \to \mu^+\mu^-\gamma$
- $\rho \to \mu^+\mu^-$
- $\omega \to \mu^+\mu^-$
- $\omega \to \mu^+\mu^-\pi^0$
- $\eta' \to \mu^+\mu^-\gamma$
- $\phi \to \mu^+\mu^-$
- $c\bar{c} \to D\bar{D} \to \mu^+\mu^- + others$
- $b\bar{b} \to B\bar{B} \to \mu^+\mu^- + others$

The decays $\omega \to \mu\mu$ and $\phi \to \mu\mu$ are known to exhibit sharp peak structures from previous lepton pair measurements, forming peaks near 0.8 GeV/c^2 and 1.0 GeV/c^2 in the mass distribution. It is known that no sharp peak structures exist for any decays other than the two-body decays of ω and ϕ. Therefore, the continuous component was fitted using an exponential function. The fitting was performed in the range of $0.5 < M_{\mu\mu} < 1.3$ GeV/c^2, excluding the regions with peak structures at $0.7 < M_{\mu\mu} < 0.86$ and $0.92 < M_{\mu\mu} < 1.15$. The continuous component was fitted using the exponential function shown (38).

$$f_{BG}(m) = N_{BG} * \exp\{-p1 * m\} \tag{38}$$

where, N_{BG} and $p1$ are the fit parameters. The continuous component mass distribution was subtracted using the results from the fit. Gaussian fits were performed for the ω and ϕ in the mass regions $0.7 < M_{\mu\mu} < 0.86$ GeV/c^2 and $0.92 < M_{\mu\mu} < 1.15$ GeV/c^2, respectively. The fitting function is given by (39) and (40).

$$f_\omega = N_\omega * \exp\left\{-\frac{1}{2}\left(\frac{m - M_\omega}{\sigma_\omega}\right)^2\right\} \tag{39}$$

$$f_\phi = N_\phi * \exp\left\{-\frac{1}{2}\left(\frac{m - M_\phi}{\sigma_\phi}\right)^2\right\} \tag{40}$$

The fit parameters are $N_\omega, N_\phi, M_\omega, M_\phi, \sigma_\omega, \sigma_\phi$. Specifically, M_ω and M_ϕ correspond to the mean mass positions of ω and ϕ, while σ_ω and σ_ϕ correspond to the mass widths. Using the fit parameters obtained from the continuous component and the Gaussian fits for ω and ϕ, all functions were combined, and a global fit was performed to extract the mean mass positions and mass widths of ω and ϕ. The fit range is $0.5 < M_{\mu\mu} < 1.3$ GeV/c^2. The function for the overall fit is given by the (41).

$$f(m) = N_{BG} * \exp\{-p1 * m\} + N_\omega * \exp\left\{-\frac{1}{2}\left(\frac{m - M_\omega}{\sigma_\omega}\right)^2\right\} + N_\phi * \exp\left\{-\frac{1}{2}\left(\frac{m - M_\phi}{\sigma_\phi}\right)^2\right\} \tag{41}$$

The parameters for the overall fit are similarly $N_{BG}, N_\omega, N_\phi, M_\omega, M_\phi, \sigma_\omega, \sigma_\phi$. The fit results are shown in Figure 16 and Table 1.

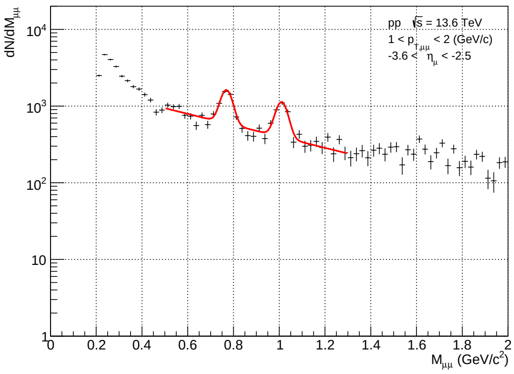

$1 < p_{T\mu\mu} < 2$ GeV/c

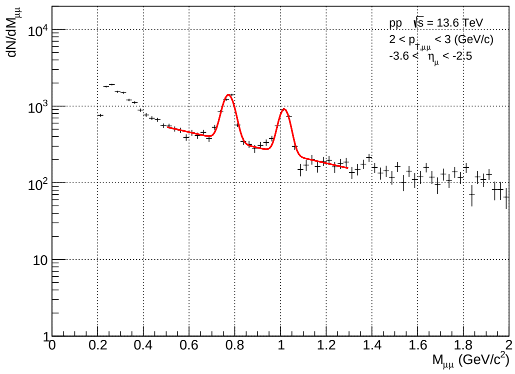

$2 < p_{T\mu\mu} < 3$ GeV/c

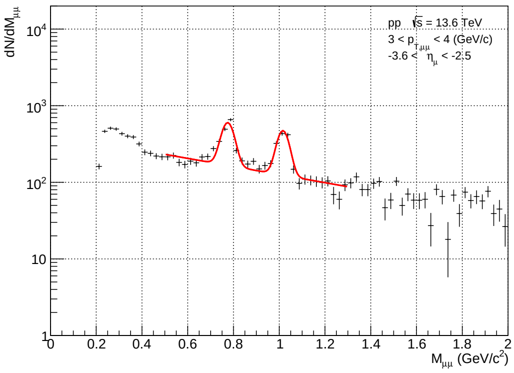

$3 < p_{T\mu\mu} < 4$ GeV/c

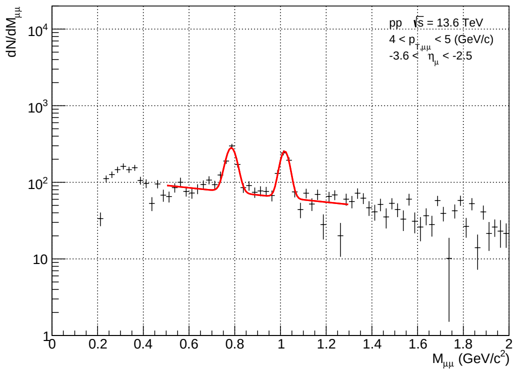

$4 < p_{T\mu\mu} < 5$ GeV/c

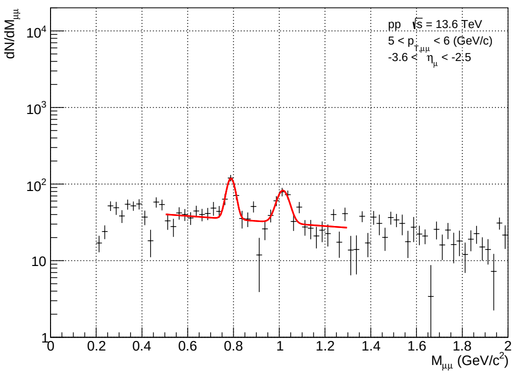

$5 < p_{T\mu\mu} < 6$ GeV/c

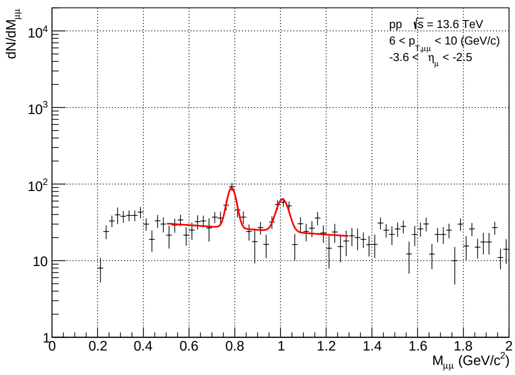

$6 < p_{T\mu\mu} < 10$ GeV/c

Figure 16: Results of fitting to the correlated invariant mass distribution obtained from Figure 15 in the region $0.5 < M_{\mu\mu} < 1.3\text{GeV}/c^2$. The red line is the result of the global fit with 41.

The mean mass positions and mass widths of ω and ϕ for each transverse momentum, as well as the χ^2 of the fit, are summarised in the following table.

3.5.4 Yield calculation of ω, ϕ

The yield for each meson was calculated using the mean mass position and mass width of $\omega \to \mu\mu$ and $\phi \to \mu\mu$ obtained from the above fit. The number of dimuons falling within 3σ of each Gaussian

Table 1: Result of fit at each transverse momentum. mean mass mass width unit is GeV/c^2. Unit of transverse momentum is GeV/c.

	ω mean mass	ω mass width	ϕ mean mass	ϕ mass width	fit χ^2
$1 < p_{T\mu\mu} < 2$	0.769 ± 0.002	0.025 ± 0.002	1.010 ± 0.002	0.026 ± 0.002	47.74/24
$2 < p_{T\mu\mu} < 3$	0.773 ± 0.001	0.026 ± 0.001	1.017 ± 0.001	0.024 ± 0.001	58.80/24
$3 < p_{T\mu\mu} < 4$	0.775 ± 0.002	0.026 ± 0.002	1.016 ± 0.002	0.025 ± 0.002	76.50/24
$4 < p_{T\mu\mu} < 5$	0.785 ± 0.002	0.024 ± 0.002	1.018 ± 0.002	0.021 ± 0.002	53.96/24
$5 < p_{T\mu\mu} < 6$	0.789 ± 0.003	0.018 ± 0.003	1.016 ± 0.005	0.026 ± 0.005	36.85/24
$6 < p_{T\mu\mu} < 10$	0.786 ± 0.003	0.019 ± 0.004	1.009 ± 0.005	0.024 ± 0.003	27.12/24

was calculated as the yield for ω and ϕ, respectively.

$$\text{min} = -3 \times \sigma + M \tag{42}$$

$$\text{max} = 3 \times \sigma + M \tag{43}$$

$$\text{Yield} = \sum_{n=\text{min}}^{\text{max}} N_n(m) \tag{44}$$

The yields for each were calculated using the mean mass positions and mass widths of $\omega \to \mu\mu$ and $\phi \to \mu\mu$ obtained from the above fit. The mass distribution was obtained by subtracting the continuous component from the dimuon mass distribution with correlations. For this mass distribution, the number of entries within three times the mass width from the mass positions of ω and ϕ were calculated as their respective yields. The calculation formula is as (44), where the mass distribution after subtracting the continuous component is denoted as $N_n(m)$. The results from the table above are presented as graphs in Figure 35 and Figure 36.

Table 2: Calculated results for ω and ϕ yields. The unit of transverse momentum is GeV/c.

	ω Yield	ϕ Yield
$1 < p_{T\mu\mu} < 2$	$(2.43 \pm 0.18) \times 10^3$	$(1.82 \pm 0.15) \times 10^3$
$2 < p_{T\mu\mu} < 3$	$(2.79 \pm 0.11) \times 10^3$	$(1.64 \pm 0.09) \times 10^3$
$3 < p_{T\mu\mu} < 4$	$(1.278 \pm 0.064) \times 10^3$	$(0.886 \pm 0.055) \times 10^3$
$4 < p_{T\mu\mu} < 5$	$(0.533 \pm 0.038) \times 10^3$	$(0.378 \pm 0.033) \times 10^3$
$5 < p_{T\mu\mu} < 6$	$(0.159 \pm 0.021) \times 10^3$	$(0.142 \pm 0.023) \times 10^3$
$6 < p_{T\mu\mu} < 10$	$(0.033 \pm 0.005) \times 10^3$	$(0.023 \pm 0.004) \times 10^3$

3.6 Analysis for improving MFT-MCH matching purity

The mass distribution of dimuons with $p_{T\mu\mu}$ below 1 GeV/c^2, which is not shown in Figure 15, is presented here. From Figure 17, the peak structures of ω and ϕ are not observed. This is due to the insufficient reconstruction resolution of η, p_T, and ϕ at low p_T for single muons. The installation of the MFT is expected to enable high-precision measurements of η and ϕ, thereby improving the reconstruction resolution of p_T through enhanced η and ϕ resolution. However, with the current reconstruction method, sufficient resolution has not been achieved, preventing the observation of the ω and ϕ peaks in the dimuon invariant mass distribution at low transverse momentum. This is likely due to challenges in matching tracks between the newly introduced MFT and the MCH, which hinder achieving adequate resolution. This chapter presents an analysis aimed at improving the MFT-MCH

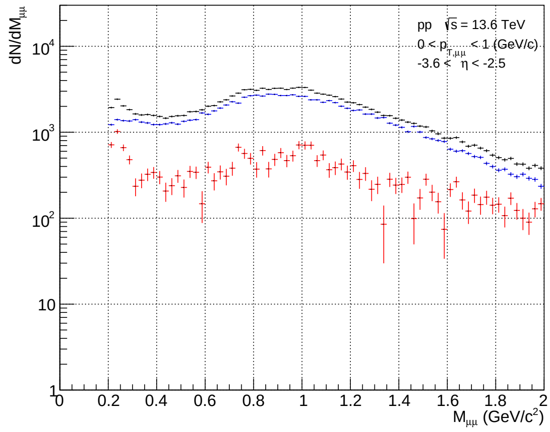

Figure 17: Combinatorial subtraction of dimuon transverse momentum $0 < p_{T\mu\mu} < 1\mathrm{GeV}/c$. Black is the reconstructed invariant mass distribution for all combinations of muons of different signs in the same event. Blue is the uncorrelated background event estimated using the Like Sign method. Red is the correlated muon vs invariant mass distribution obtained by subtracting blue from black.

matching purity across all transverse momentum distributions, rather than restricting the focus to low p_T.

3.6.1 MFT-MCH matching χ^2 optimization

Using the yield analysis method for $\omega \to \mu\mu$ and $\phi \to \mu\mu$ described in 3.5.2-3.5.4, the MFT-MCH matching χ^2 cut value for single muon tracks was optimised to maximise signal detection efficiency. The MFT-MCH matching χ^2 value represents the parameter difference when extrapolating MFT and MCH tracks to the matching plane. A larger χ^2 value indicates more fake matches, whereas a smaller value corresponds to more correct matches. Fake match tracks can be removed by applying a cut on this value. However, optimising the cut to minimise fake matches while preserving as many correct matches as possible is necessary. In this study, the optimisation was performed by maximising the signal significance using the peaks of $\omega \to \mu\mu$ and $\phi \to \mu\mu$. The signal was calculated by performing the same analysis as in 3.5.2, 3.5.3, and 3.5.4 for the mass distributions in all transverse momentum regions. The number of background was determined by counting the entries in the background-subtracted mass distribution within the same mass window used for signal calculation, and this was used as the background estimate. The significance, $S/\sqrt{S+BG}$, was then calculated. This calculation was performed for mass distributions reconstructed using only muons with an MFT-MCH matching χ^2 below a given threshold. Figure 18 presents the results of the combinatorial background subtraction after applying the χ^2 cut. Similar to Figure 15, the black histogram represents the mass distribution reconstructed from all oppositely charged muon pairs in the same event. The blue histogram represents the combinatorial background estimated using the Like-Sign method. The red histogram corresponds to the background-subtracted distribution, representing the invariant mass distribution of correlated dimuons.

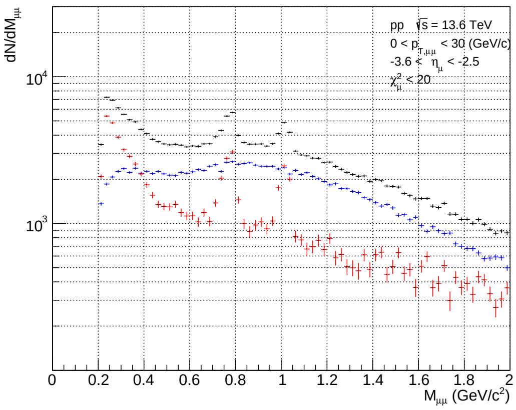

MFT-MCH matching $\chi^2 < 20$

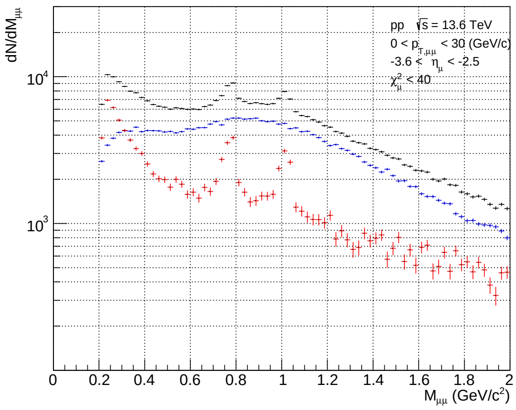

MFT-MCH matching $\chi^2 < 40$

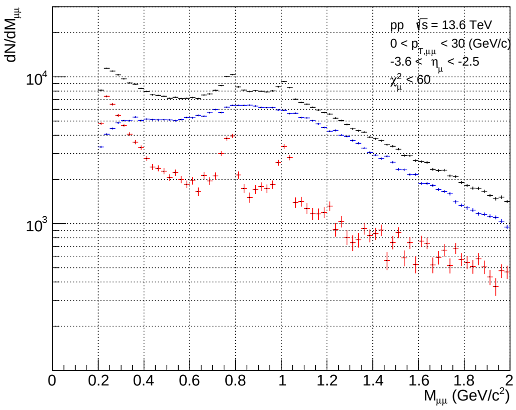

MFT-MCH matching $\chi^2 < 60$

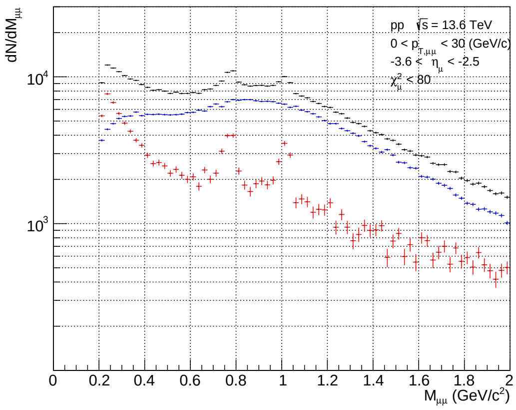

MFT-MCH matching $\chi^2 < 80$

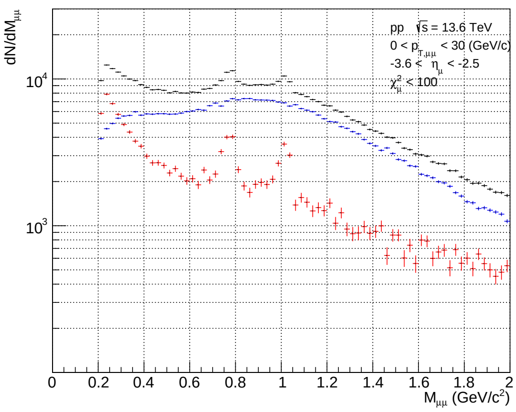

MFT-MCH matching $\chi^2 < 100$

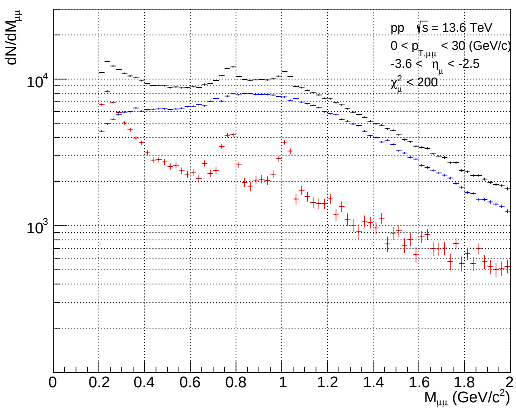

MFT-MCH matching $\chi^2 < 200$

Figure 18: The result of Combinatorial Background subtraction after applying the MFT-MCH matching χ^2 cut. Black is the reconstructed invariant mass distribution for all combinations of muons of different signs in the same event. Blue is the uncorrelated background event estimated using the Like Sign method. Red is the correlated muon vs invariant mass distribution obtained by subtracting blue from black.

The black distribution decreases in size by reducing the χ^2 cut. Additionally, it can be observed that the ω and ϕ peaks in the red distribution become more pronounced. Figure 19 shows the fitting results for this red distribution.

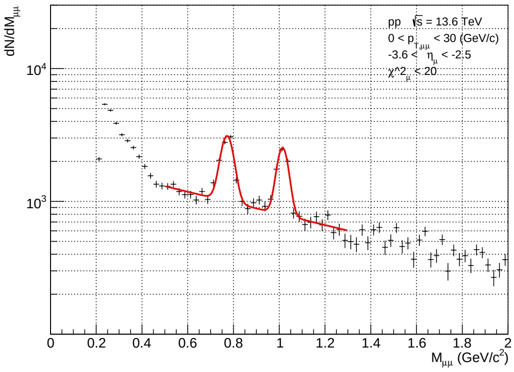

MFT-MCH matching $\chi^2 < 20$

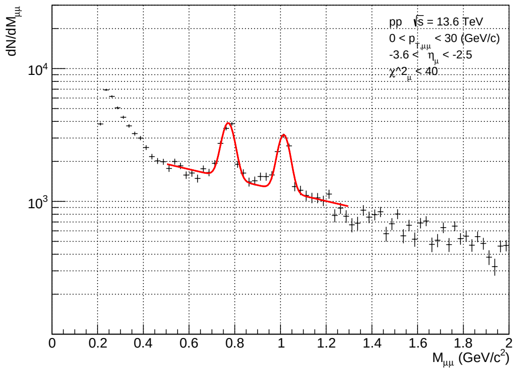

MFT-MCH matching $\chi^2 < 40$

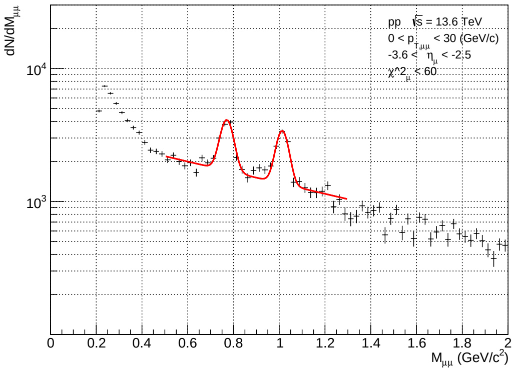

MFT-MCH matching $\chi^2 < 60$

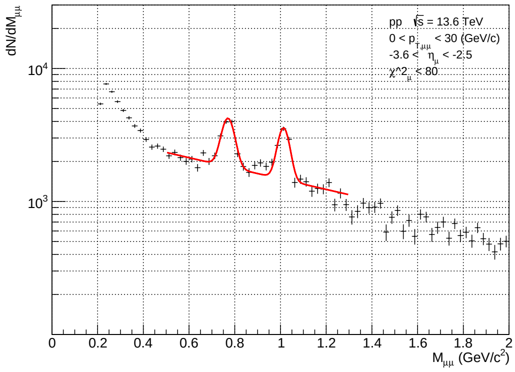

MFT-MCH matching $\chi^2 < 80$

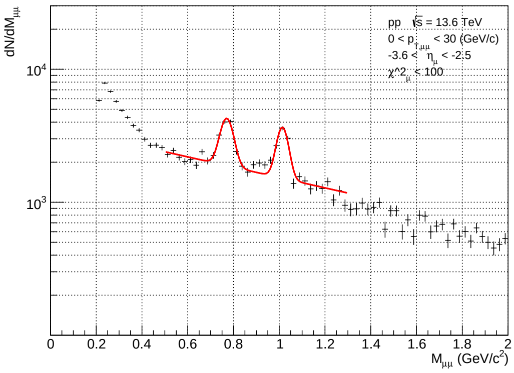

MFT-MCH matching $\chi^2 < 100$

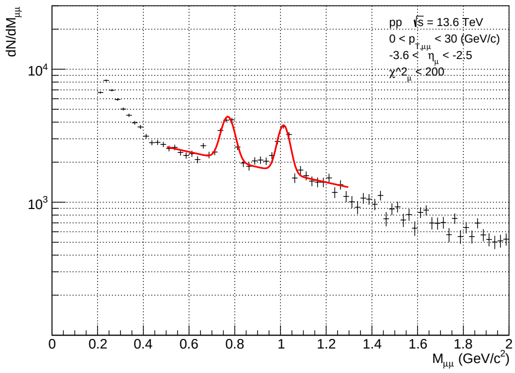

MFT-MCH matching $\chi^2 < 200$

Figure 19: Results of fitting to the correlated invariant mass distribution obtained from Figure 18 in the region $0.5 < M_{\mu\mu} < 1.3\text{GeV}/c^2$. The red line results from the global fit with (41).

Figure 20 and Figure 21 show the χ^2 dependence of $S/\sqrt{S+BG}$ obtained in the fit. The horizontal axis represents the matching χ^2, while the vertical axis shows $S/\sqrt{S+BG}$. As the cut value is reduced, the value of $S/\sqrt{S+BG}$ increases. When a cut of $\chi^2 < 30$ is applied, $S/\sqrt{S+BG}$ reaches its maximum for both ω and ϕ. From this result, it is evident that the optimal matching χ^2 value is

$\chi^2 < 30$.

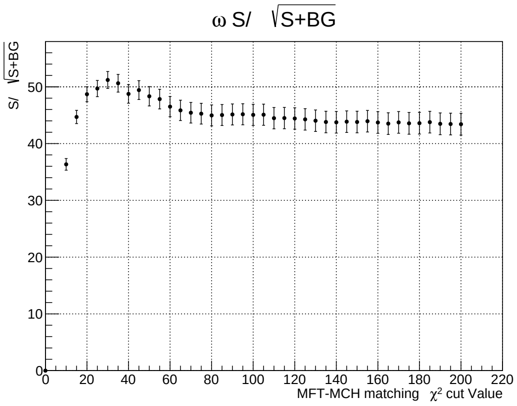

Figure 20: ω significance

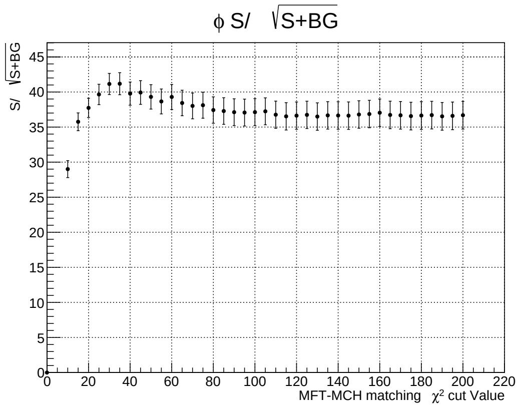

Figure 21: ϕ significance

3.6.2 Fake match track removal analysis of Global Track using MFT Track η - MCH Track η

The η distribution of Global Tracks differs significantly from the true distribution. This discrepancy arises due to muon reconstruction involving the MFT, indicating issues with MFT-MCH matching. Fake matches contribute to this significantly distorted η distribution. By removing these distortions, it is shown that the resolution of η, p_T, and ϕ for single muons improves. In this analysis, Fake matches are removed by utilising the difference in η between the MFT Track and MCH Track that constitute the Global Track. The dataset used is LHC24b1, which consists of Monte Carlo data of proton-proton collisions at $\sqrt{s} = 13.6$ TeV from minimum-bias events. This simulation data has been compared with real data, confirming that they exhibit the same behaviour.

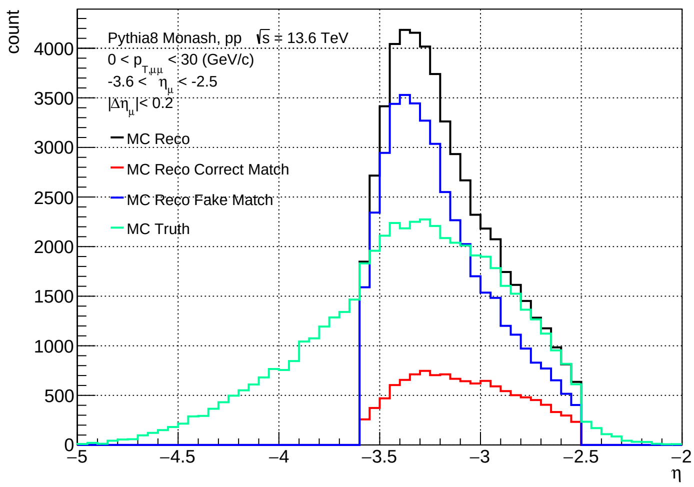

Figure 22: Black is the η distribution of Global Track, red is the η distribution of correct match tracks, and blue is the η distribution of fake match tracks. Moreover, green is the true η distribution corresponding to black.

Figure 22 shows the η distribution of Global Tracks for all p_T regions. The black histogram represents the reconstructed η distribution of Global Tracks. The blue histogram corresponds to the η distribution of reconstructed tracks identified as Fake matches, while the red histogram represents the η distribution of correctly matched tracks. The green histogram represents the true η distribution corresponding to the black reconstructed tracks. Comparing the black reconstructed muon distribution with the green true distribution, the acceptance range of Global Tracks is $-3.6 < \eta < -2.5$. However, in the green distribution, muons with η values smaller than -3.6 are reconstructed within the $-3.6 < \eta < -2.5$ range. This phenomenon is likely caused by muons that passed through the absorber and subsequently traversed the MCH-MID system while being outside the MFT acceptance. To remove such tracks, a $\Delta\eta$ cut is applied as (45).

$$\Delta\eta = \text{MFT Track}\,\eta - \text{MCH Track}\,\eta \tag{45}$$

For each track, $\Delta\eta$ was calculated. Figure 23 shows the distribution. The black represents the distribution of reconstructed muons, the blue represents the distribution of Fake match tracks, and the red represents the distribution of Correct match tracks.

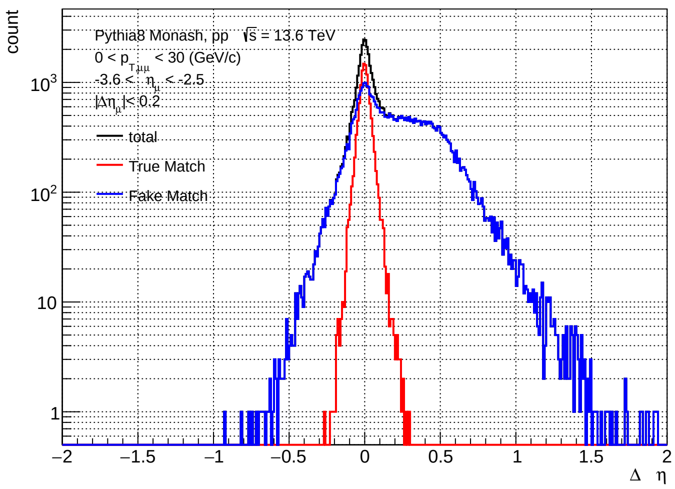

Figure 23: $\Delta\eta$ distribution of Global Track. Black is the $\Delta\eta$ distribution of the reconstructed Global Track, red is the $\Delta\eta$ distribution of the tracks that are correct matches among them, and blue is the $\Delta\eta$ distribution of the tracks that are fake matches.

For $|\Delta\eta| > 0.2$, Fake Match tracks dominate. The distributions and resolutions of each physical quantity are shown by applying a $|\Delta\eta| < 0.2$ cut to remove Fake matches while retaining as many Correct matches as possible.

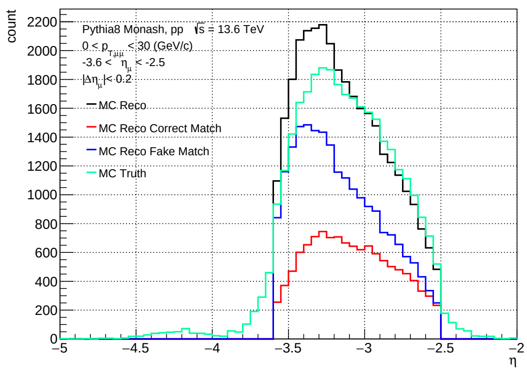

Figure 24: The η distribution of Global Tracks after the $\Delta\eta$ cut

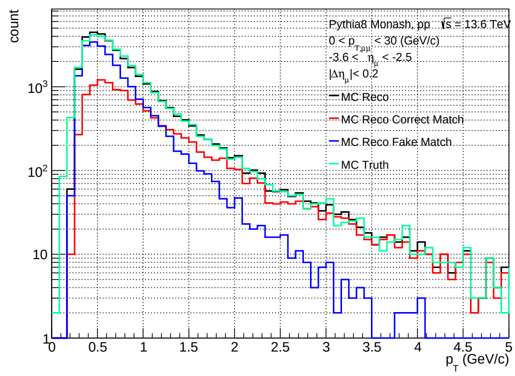

Figure 25: The p_T distribution of Global Tracks after the $\Delta\eta$ cut

Figure 24 shows the η distribution after the $\Delta\eta$ cut. Additionally, Figure 25 displays the p_T distribution after the $\Delta\eta$ cut. As in Figure 22, the black histogram represents all reconstructed muon tracks, the red represents Correct match tracks, and the blue represents Fake Match tracks. The green histogram corresponds to the true η distribution for the black muons. Comparing the green distribution of η after the cut with Figure 22, we see that the muons distributed at $\eta < -3.8$ have been removed. Furthermore, this cut removes many Fake match tracks in the range of $-3.6 < \eta < -3.2$. However, as seen from Figure 25, Fake matches originating from low transverse momentum remain.

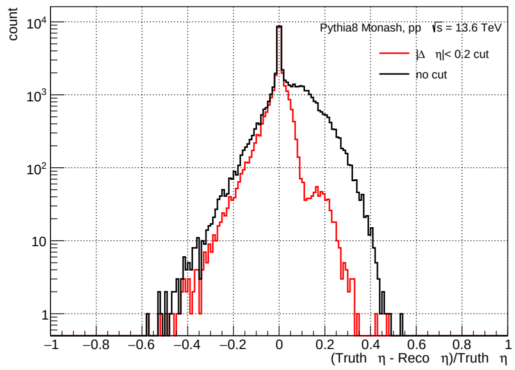

Figure 26: Resolution of η

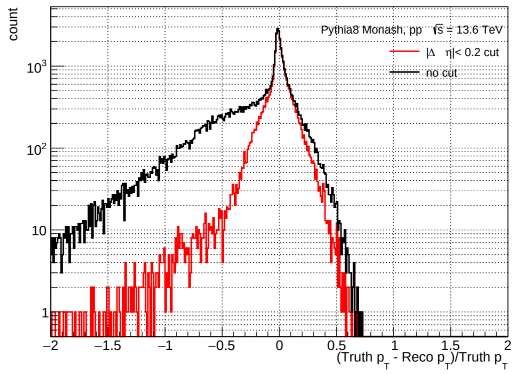

Figure 27: Resolution of p_T

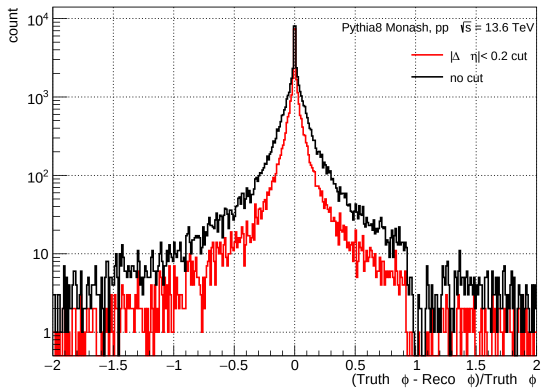

Figure 28: Resolution of ϕ

Figures 26, 27, and 28 show the resolution of p_T, η, and ϕ, respectively. The horizontal axis represents the resolution, calculated by subtracting the reconstructed quantity from the true physical quantity and dividing it by the true value. The vertical axis represents the count. The black distribution shows the resolution without applying the $\Delta\eta$ cut, while the red distribution shows the tracks after applying the $|\Delta\eta| < 0.2$ cut. By comparing the black and red histograms, it is clear that the resolution has a small value for all distributions. This shows that the resolution improves with the cut. Next, we will describe the efficiency and matching purity improvements due to the cut. The $|\Delta\eta| < 0.2$ cut was applied in such a way as to discard as few correct match tracks as possible while removing fake match tracks. For the p_T distribution, the efficiency drops below 2 (GeV/c), but the matching purity improves. The product of efficiency and purity remains unchanged compared to before the cut. This indicates that the cut does not significantly remove correct matches. For the η distribution, efficiency is reduced in the range $-3.6 < \eta < -3$, but matching purity improves in the

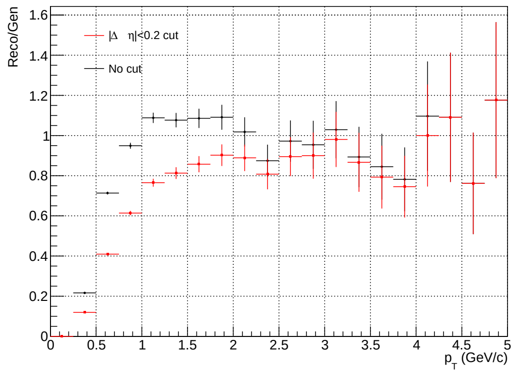

Figure 29: Efficency of p_T

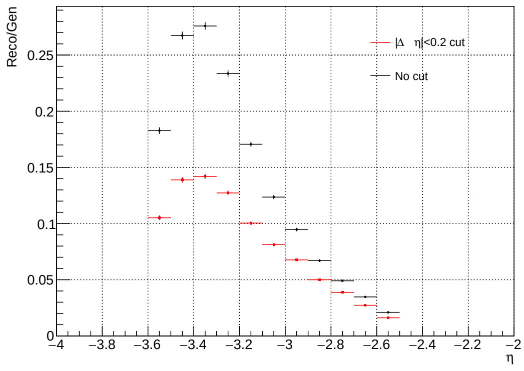

Figure 30: Efficency of η

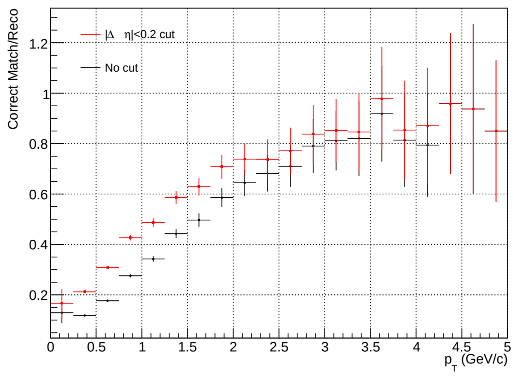

Figure 31: Purity of p_T

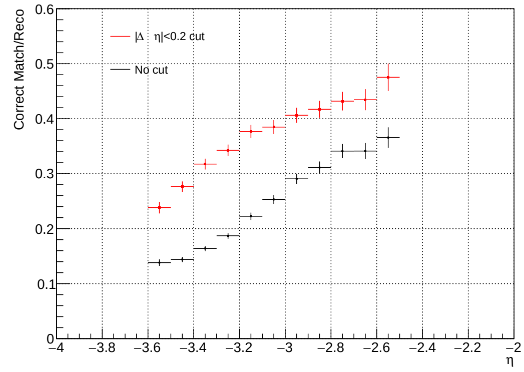

Figure 32: Purity of η

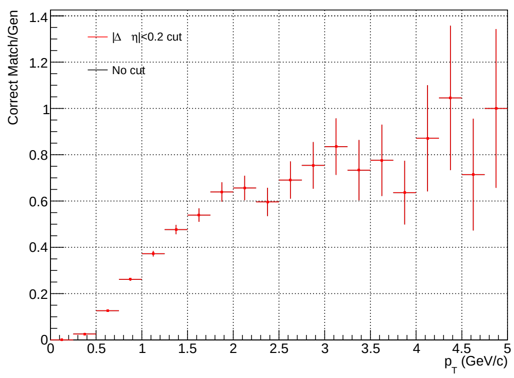

Figure 33: Efficency × Purity of p_T

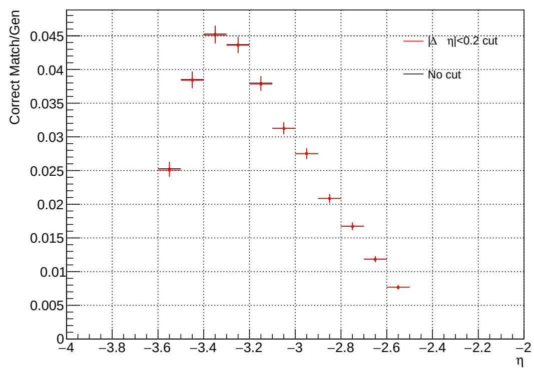

Figure 34: Efficency × Purity of η

range $-4 < \eta < -2$. Similarly, the product of efficiency and purity for η also remains unchanged compared to before the cut.

4 Results and Discussion

This chapter presents the graphs of the ω and ϕ row yields calculated in 2 as the conclusion. Figure 35 and Figure 36 show the transverse momentum spectra of the production yields of ω and ϕ. The horizontal axis represents the transverse momentum of ω and ϕ, while the vertical axis represents the number of counts. Since these spectra are uncorrected, no physical discussion can be made. However, it is observed that the yields decrease as the transverse momentum increases. Here, it is necessary to consider the contribution of $\rho \to \mu\mu$. The ρ meson has a mean mass of $m = 775.26$ MeV and a full width of $\Gamma = 149.1$ MeV, leading to a broader distribution than ω, which is located at a very similar mass position. Given that the signal extraction method used in this analysis accounts for the broad width of the ρ, it is considered that the peak structure of ω is not significantly affected.

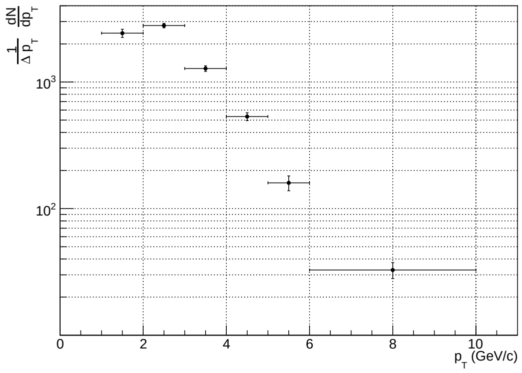

Figure 35: ω yield

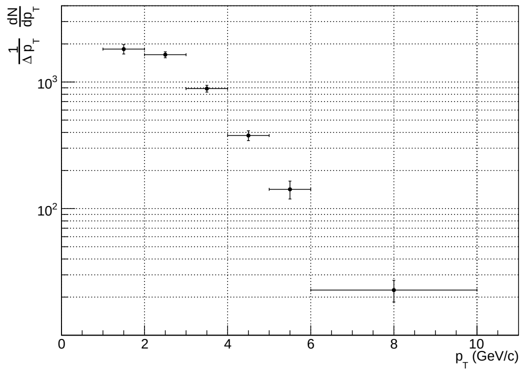

Figure 36: ϕ yield

4.1 Prospect of ω and ϕ cross section measurement

As a future perspective, I will use the yields of $\omega \to \mu\mu$ and $\phi \to \mu\mu$ calculated by Figure 35 and Figure 36 to calculate the ω and ϕ. I aim at the transverse momentum spectrum of the production cross-section. (46) can calculate the production cross-section[11].

$$\frac{d^2\sigma}{dydp_T} = \frac{1}{\Delta y \Delta p_T} \times \frac{N(\Delta p_T, \Delta y)}{[Acc \times Eff](\Delta p_T, \Delta y) \times BR_{\phi,\omega\to\mu\mu} \times L_{int}} \tag{46}$$

where,$[Acc \times Eff](\Delta p_T, \Delta y)$ is the acceptance efficiency correction factor for $\omega \to \mu\mu, \phi \to \mu\mu$, BR is the branching ratio of $\omega \to \mu\mu, \phi \to \mu\mu$, L_{int} is the integrated luminosity. Acceptance efficiency correction was performed using Monte Carlo simulations with a forward detector group of $\omega \to \mu\mu, \phi \to \mu\mu$. It can be obtained by calculating the ratio of the number reconstructed/number generated. With this correction, the generated cross-section of ω, ϕ can be derived by calculating the integrated lumminosity and Branching Ratio. Therefore, as a prospect, I will use Monte Carlo simulation to obtain the generating cross section of ω, ϕ with the acceptance-efficiency correction. This will enable the calculation of production cross-sections from the present results, allowing for comparison with Run 2 results. I will compare the generated cross sections of ω, ϕ measured in Run 2 in the trajectory, including MFT and investigate the quality of the trajectory reconstruction in Run 3.

4.2 Single muon track resolution improvements

Discuss single muon track reconstruction, 3.6, and prospects. In the current muon track reconstruction algorithm, the η and ϕ of the muon are determined using the MFT Track to improve their precision. However, the DCA is calculated using parameters obtained from the global fit of the Global Track. Since using tracks closer to the collision point allows for more precise measurements unaffected by the absorber, it is expected that the accuracy of the DCA measurement can be improved by using the parameters of the MFT track that constitutes the Global Track. Furthermore, improvements in MFT-MCH matching are also needed. As seen in Figure 31, the matching purity significantly decreases at low p_T. This degradation occurs because low p_T muons undergo multiple scattering and energy loss in the absorber, making MFT-MCH matching more challenging. However, this study demonstrated that applying a $\Delta\eta$ cut improves matching purity in the low p_T region. This result suggests that continued analysis can further enhance matching purity. As a prospect, improving the resolution of single muon kinematic variables will enhance the mass resolution, making the ω peak sharper and allowing better separation between the ρ and ω peaks.

4.3 Search for chiral symmetry restoration

The ultimate goal is to measure the changes in the mass distribution of light vector mesons in lead-lead collision events. This study has revealed several remaining challenges, including issues with matching purity at low transverse momentum and the development of the track reconstruction algorithm. Another challenge is improving the quality of muon tracks in high-multiplicity events in heavy-ion collisions. As a first step, efforts will be focused on improving matching purity and developing the track reconstruction algorithm in proton-proton collisions, where the event multiplicity is relatively low. Subsequently, similar improvements will be pursued in heavy-ion collisions. Going forward, the aim is to clarify the changes in the mass distribution of light vector mesons due to QGP formation and observe the restoration of chiral symmetry.

5 Summary

In this study, I analyzed forward muon pairs in ALICE from $\sqrt{s} = 13.6$ TeV pp collisions. The peaks corresponding to $\omega \to \mu\mu$ and $\phi \to \mu\mu$ in the dimuon mass distribution were extracted with Gaussian functions. In contrast, other components were fitted with an exponential function. These analyses were performed for each transverse momentum range, and the transverse momentum spectra of ω and ϕ yields were presented. Additionally, an analysis was conducted to improve the purity of the matching MFT and MCH. By applying a cut on the difference in η between the MFT Track and the MCH Track that constitute the Global Track, we demonstrated the ability to remove Fake match tracks. Furthermore, the optimal MFT-MCH matching χ^2 cut was determined using the signal yields of ω and ϕ. As a prospect, further improvements in the quality of single muon tracks will be pursued. Ultimately, this study aims to clarify the changes in the mass distribution of light vector mesons caused by the formation of the QGP in lead-lead nuclear collisions.

6 Acknowledgements

I want to thank everyone involved in this study.

First of all, Prof. Kenta Shigaki, thank you very much for not only your daily guidance but also for giving me various opportunities to present my research and to learn at research meetings and academic conferences. Those experiences helped me gain basic knowledge of the ALICE experiment and of heavy ion collision experiments as a whole.

Prof. Yorito Yamaguchi. Thank you very much for all your comments on the plots during the analysis process, especially at the meeting. Thanks to your help, I developed my ability to think logically and proceed with my research, even though it is still in its infancy.

Prof. Satoshi Yano, thank you very much for your opinions on muon analysis. I learned the importance of thinking about the analysis necessary for current muon analysis and planning for the future.

Prof. Keisuke Homma, Prof. Miyoshi, thank you very much for your questions and suggestions in the weekly lab meetings, business trip reports, midterm presentations, and so on. Through your questions and suggestions, I learned about your attitude toward research.

Mr. Motomi Oya, thank you very much for teaching me the method of forward muon pair analysis from scratch. Your wide-ranging opinions, from consultation on research policy to debugging the analysis code, helped me advance my research. As a senior student with the highest grade in the laboratory, I have had many occasions to learn from you.

Mr. Kento Kimura, thank you very much for consulting with me on many aspects of my research policy. Your knowledge of the theory of lepton pair measurement has greatly advanced my understanding of this research.

To everyone in the laboratory: Thank you for your daily involvement, from opinions about the contents of this research to refreshing chats.

To the ALICE experimental group. This study was analyzed using data acquired by the ALICE collaboration. Once again, I would like to express my gratitude.

Dr, Sarah, Dr. Batoul, Dr. Maurice and Dr. Luca for their appropriate comments during my presentations at the MFT meeting and the DQtomumu PAG meeting. These comments helped me understand what was missing in my analysis and what I needed to think about.

References

[1] S. Navas *et al.* [Particle Data Group], Phys. Rev. D **110**, no.3, 030001 (2024) doi:10.1103/PhysRevD.110.030001

[2] W. Weise, Nucl. Phys. A **553**, 59C-72C (1993) doi:10.1016/0375-9474(93)90615-5

[3] A. Maire, Phase diagram of QCD matter: Quark-Gluon Plasma, 2015. Available at: https://cds.cern.ch/record/2025215

[4] ALICE Collaboration., Acharya, S., Adamová, D. et al. The ALICE experiment: a journey through QCD. Eur. Phys. J. C 84, 813 (2024). https://doi.org/10.1140/epjc/s10052-024-12935-y

[5] F. Geurts and R. A. Tripolt, Prog. Part. Nucl. Phys. 128, 104004 (2023) doi:10.1016/j.ppnp.2022.104004

[6] S. Acharya*et al.* [ALICE], "Dielectron production in central Pb−Pb collisions at $\sqrt{s_{\rm NN}} = 5.02$ TeV," [arXiv:2308.16704 [nucl-ex]].

[7] R. Rapp and J. Wambach, Adv. Nucl. Phys. **25**, 1 (2000) doi:10.1007/0-306-47101-9_1 [arXiv:hep-ph/9909229 [hep-ph]].

[8] S. Damjanovic *et al.* [NA60], Nucl. Phys. A **783**, 327-334 (2007) doi:10.1016/j.nuclphysa.2006.11.015 [arXiv:nucl-ex/0701015 [nucl-ex]].

[9] "Technical Design Report for the Muon Forward Tracker," CERN-LHCC-2015-001, ALICE-TDR-018, 2015. Available at

[10] "ALICE dimuon forward spectrometer: addendum to the Technical Design Report" CERN-LHCC-2000-046,Technical design report. ALICE, 2000. Available at https://cds.cern.ch/record/494265

[11] S. Acharya et al. [ALICE Collaboration], Eur. Phys. J. C 81, 772 (2021) doi:10.1140/epjc/s10052-021-09545-3